J. Fluid Mech. (2011), *vol.* 677, *pp.* 63–102.
doi:10.1017/S0022112011000620

Feedback control of three-dimensional optimal disturbances using reduced-order models

ONOFRIO SEMERARO†, SHERVIN BAGHERI, LUCA BRANDT AND DAN S. HENNINGSON

Linné Flow Centre, KTH Mechanics, SE-100 44 Stockholm, Sweden

(Received 17 May 2010; revised 16 November 2010; accepted 2 February 2011; first published online 29 March 2011)

The attenuation of three-dimensional wavepackets of streaks and Tollmien–Schlichting (TS) waves in a transitional boundary layer using feedback control is investigated numerically. Arrays of localized sensors and actuators (about 10–20) with compact spatial support are distributed near the rigid wall equidistantly along the spanwise direction and connected to a low-dimensional ($r = 60$) linear quadratic Gaussian controller. The control objective is to minimize the disturbance energy in a domain spanned by a number of proper orthogonal decomposition modes. The feedback controller is based on a reduced-order model of the linearized Navier–Stokes equations including the inputs and outputs, computed using a snapshot-based balanced truncation method. To account for the different temporal and spatial behaviour of the two main instabilities of boundary-layer flows, we design two controllers. We demonstrate that the two controllers reduce the energy growth of both TS wavepackets and streak packets substantially and efficiently, using relatively few sensors and actuators. The robustness of the controller is investigated by varying the number of actuators and sensors, the Reynolds number and the pressure gradient. This work constitutes the first experimentally feasible simulation-based control design using localized sensing and acting devices in conjunction with linear control theory in a three-dimensional setting.

Key words: boundary layer stability, control theory, flow control

1. Introduction

In recent years, industrial, economical and environmental needs have reinvigorated the interest in practical methods for control of transitional and fully turbulent wall-bounded shear flows. Currently, research efforts are devoted to the manipulation of fluids by passive means, for example by riblets (Choi, Moin & Kim 1993) or discrete roughness elements (White & Saric 2000), by *ad hoc* active means, for example via wave cancellation (Sturzebecher & Nitsche 2003), opposition control (Hammond, Bewley & Moin 1998) or wall-motion techniques (Quadrio & Ricco 2004) and with linear and nonlinear control theoretical approaches, for example using spatially localized convolution kernels (Högberg, Bewley & Henningson 2003*a*) or adjoint-based optimization methods (Bewley, Moin & Temam 2001). Significant efforts are also devoted to the development of acting and sensing devices, such as synthetic jets (Smith & Glezer 1998), electro-magnetic actuators (Pang & Choi 2004),

† Email address for correspondence: onofrio@mech.kth.se

plasma actuators (Grundmann & Tropea 2008) or various micro-electro-mechanical system (MEMS) actuators (Ho & Tai 1998) constructed using micro-machining techniques.

1.1. *Linear control of transition*

It is now well established that under certain conditions, the initial phase of the laminar–turbulent transition in wall-bounded flows is largely governed by linear mechanisms. We therefore believe that tools of linear control theory may provide efficient, robust and feasible controllers to delay transition to turbulence. The combination of linear systems and control theoretical tools and transition control dates back to the seminal works by Joshi, Speyer & Kim (1997), Cortelezzi *et al.* (1998) and Bewley & Liu (1998), who paved the way for future researchers. These investigations applied feedback control to the problem of linearized plane Poiseuille flow, taking into account unknown and variable disturbances in imprecise flow conditions, mathematical modelling of boundary actuation (blowing and suction at the wall), optimality and robustness (LQG/$\mathscr{H}_\infty$ methods), minimal realizations (controllability and observability) and so on.

However, the tools in linear control theory are developed for systems with number of degrees of freedom of the order of 10^2; controllers with 10^5 of states or more are of no interest in engineering applications due to the amount of hardware and computer resources required to compute a real-time control law. As a consequence, all model-based control designs involve the problem of reducing the order of the controller. In fact, this issue was already addressed by Cortelezzi *et al.* (1998); they analysed distributed measurements and actuators and designed the linear controllers in Fourier space, since for spatially invariant systems such as channel flow, the three-dimensional (3D) system becomes completely decoupled into a set of two-dimensional (2D) subsystems. The approach requires an online 2D (for each xy-plane) fast fourier transform (FFT) of the measurement vector and an online 2D iFFT of the control vector, in addition to assuming that the disturbances are spatially periodic in the spanwise direction. However, the main drawback besides the periodicity assumption is that the cost of the online 2D FFTs grows rapidly with the number of actuators and sensors.

A different approach in physical space was adopted by Högberg & Bewley (2000) and Högberg *et al.* (2003*a*), after the theoretical predictions by Bamieh, Paganini & Dahleh (2002). There, it was shown that for spatially invariant systems with distributed control and measurements, optimal and robust controllers, obtained by solving a set or family of smaller problems in the Fourier space, are spatially localized with compact support. This means that controllers designed in Fourier space for each wavenumber pair independently (considering for example the channel flow) result in realizable and practicable controllers (or kernels) in *physical space*, which can at least hypothetically be implemented using MEMS. Several successful projects were initiated to extend this approach to weakly spatially developing flows (Chevalier *et al.* 2007*a*; Monokrousos *et al.* 2008) and even to fully turbulent flows (Högberg, Bewley & Henningson 2003*b*; Chevalier *et al.* 2006). However, there are several shortcomings of this approach which have rendered it difficult to implement it experimentally: (i) it introduces a controller with the same order as the plant; (ii) it is only applicable to spatially invariant systems; (iii) it assumes distributed sensors and actuators.

As we mentioned earlier, controllers of very high order are useless in applications; today we lack methods to reduce the order of very high-dimensional controllers in a

systematic way, since the methods developed in the control community are applicable only to moderate size controllers. The limitation to spatially invariant flows is a severe restriction; even if the approach can be extended to weakly spatially developing flows, more complex flows such as flows in ducts, corners, diffusers and around leading edges are out of reach. Finally, the assumption of distributed sensors and actuators restricts the approach to acting and sensing devices that can be manufactured in very large numbers such as MEMS devices; in many applications this is not cost-efficient and, moreover, only a few localized sensors and actuators are suffice to manipulate the flow in a desired way.

1.2. *Model reduction of the Navier–Stokes equations*

This paper addresses the limitations – with no assumptions made about the geometry or about the shape and distribution of actuators and sensors – of previous methods in a direct and efficient way by reducing the complexity of the Navier–Stokes equations before designing the controller. For this model reduction step to be meaningful, the complexity of the governing system must be reduced by several orders of magnitude, that is, from several million degrees of freedom to less than a hundred, while preserving the essential dynamics. It has not been clear how to define 'essential dynamics' in the context of transition control and once defined, if such an enormous order reduction can be performed in a systematic and efficient manner. The method used in this paper is balanced truncation. An approximation of this approach for large-scale systems, such as those typical in fluid mechanics, was proposed by Rowley (2005) and recently applied to channel flow instabilities by Ilak & Rowley (2008).

As recognized by Bewley (2001), the only requirement to achieve the desired flow behaviour is that suitable control signals are determined based only on filtered information delivered from the sensor measurement. Thus, of utmost importance for control design is to extract the components necessary to describe the relation among *time signals* from the full dynamics governed by Navier–Stokes equations. A general input–output framework was developed in Bagheri, Brandt & Henningson (2009*b*), where the disturbance and actuators were considered as inputs, whereas the objective function and sensors were considered as outputs. It was shown that the input–output behaviour is the 'essential dynamics' and it could be represented equally well with a reduced-order model of 60 degrees of freedom as with the Navier–Stokes equations of order 10^5. This proof-of-concept work showed for the first time that this significant order reduction can be combined with control theoretical tools to attenuate disturbances in spatially developing flows. The work presented in this paper extends previous research on reduced-order models and linear feedback control of 2D disturbances to a fully 3D setting. This is not a trivial extension, since the third spatial direction introduces several new challenges; the disturbance dynamics is significantly more complex due to the presence and competition of different instability mechanisms.

When the background disturbance level is very low (of the order of 0.05 %), packets of travelling waves, Tollmien–Schlichting (TS) waves, are typically observed in boundary layers. These waves are characterized by small streamwise scales and large spanwise extent. However, in the presence of moderate levels of vortical perturbations in the free stream, streaky streamwise-elongated structures emerge in the boundary layer; these streaks have a dominant spanwise length scale of the order of the boundary-layer thickness.

In addition to having completely different spatial structures, these two disturbances also evolve on different time scales. The TS wavepackets grow exponentially on a viscous time scale and break down when they reach amplitudes of the order of a few per cent of the free-stream velocity, whereas the streaks grow at an algebraic rate, quickly reaching their peak energy and triggering turbulence at amplitudes one order of magnitude larger than TS wavepackets. The two types of disturbances span a wide range of temporal and spatial scales, making the control design and in particular the choice of actuators and sensors and their placement a disturbance-dependent task. Indeed, previous work on flow control has targeted either streaks or TS wavepackets; however, in realistic conditions, it is likely that both instability mechanisms co-exist. In order to be able to control both types of disturbances, we build two controllers: each aimed at one of the two types of instabilities. However, it is the intention of this work to control both types of disturbances using the same spatial shape of actuators and sensors.

1.3. *Scope of the investigation*

The present study is based on a fully 3D configuration that resembles actual experimental set-ups – see for instance Lundell (2007) or Sturzebecher & Nitsche (2003) – with a set of localized actuators and sensors distributed near the wall. The long-term aim of this research project is to develop numerically reliable and fast controllers that are possible to use in laboratory experiments. For example, measurements from hot film sensors or wall wires could, after being processed by analogue to digital converters (A/D) and digital signal processors (DSP), be fed to a computer that quickly computes the control signals using the numerically obtained low-order controller developed in this work. The control signal would then be converted to analogue signal using D/A converter and fed to plasma actuators. Numerical investigations can also be useful for wind-tunnel experiments, by providing guidelines for the shape and spatial distribution of actuators and sensors. The design and placement of actuators and sensors can be studied through extensive numerical parametric studies, reducing the number of experiments required to obtain a satisfactory controller. Thus, we believe that the numerical study presented here takes us one step closer to incorporating theoretical tools into the practical (experimental) flow control community.

The objective of this work is to investigate whether 3D streaks and TS wavepackets can be attenuated by specific controllers based on a few localized sensors and actuators. The controllers are designed using reduced-order models in conjunction with linear optimal feedback control. In addition, the efficiency and robustness of the linear controller will be investigated to assess the control performance when the system is operating at off-design conditions.

This paper is organized as follows. In §§ 2 and 3, the control problem is formulated with a description of the configuration, disturbances, actuators, sensors and objective functions. The model reduction problem is briefly introduced. The characterization of the leading balanced modes and the validation of the reduced-order models of the Navier–Stokes system are provided in § 4. In this section, we start by discussing separately the results for streaks and TS waves, while the previous theoretical formulation is independent of the specific disturbance considered. Section 5 provides a short introduction to the linear quadratic Gaussian (LQG) framework. Sections 6 and 7 contain the main results of the paper: the performance of the control is evaluated for 11 different configurations of sensors and actuators for the TS wavepackets case

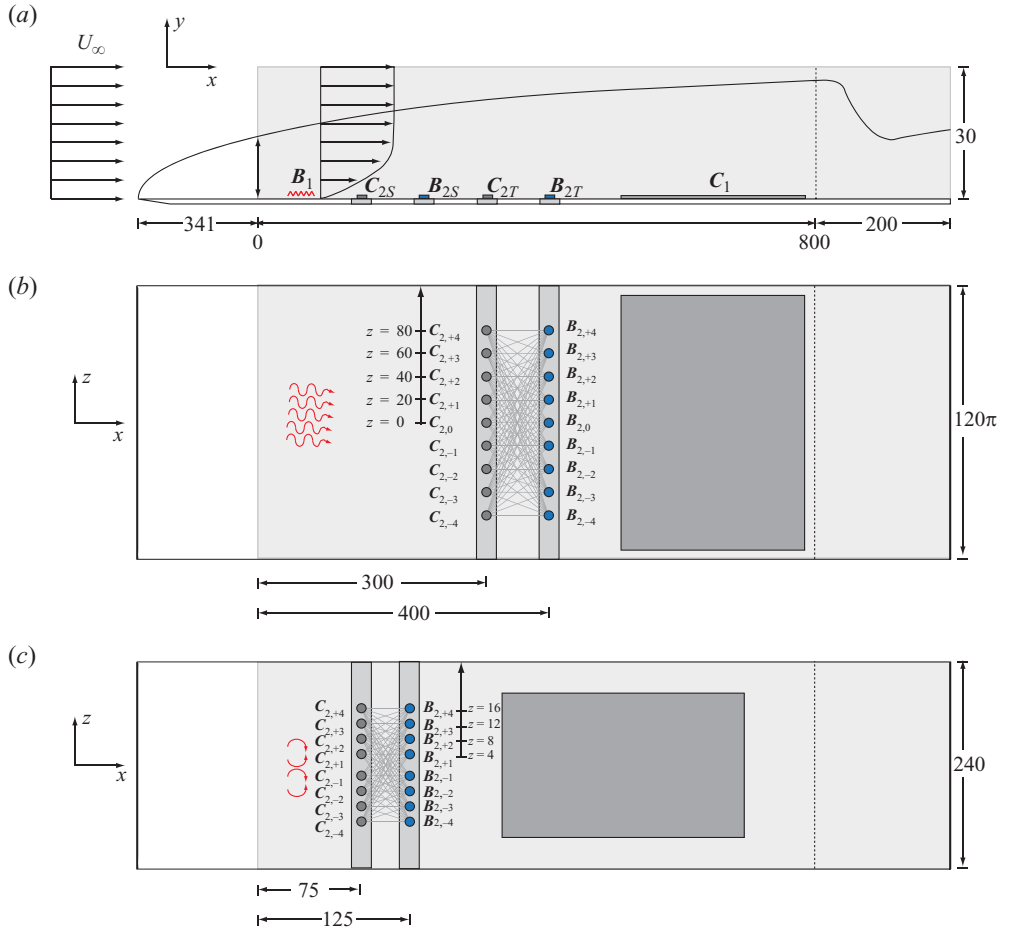

FIGURE 1. Input–output configurations. For a complete list of the cases, see tables 1 and 2. Here the side view (*a*), the reference cases for the TS case (*b*) and the streak case (*c*) are depicted. The input $\boldsymbol{B}_1$ in (*b*) is an optimal initial condition that triggers TS waves, located at (30, 1, 0). The control action is provided by the input $\boldsymbol{B}_2$, which consists of a row of actuators located at $x = 400$. The output $\boldsymbol{C}_2$ at $x = 300$ contains an array of sensors used for flow estimation. For the streak case (*c*), $\boldsymbol{B}_1$ is located at (30, 1, 0), $\boldsymbol{B}_2$ at $x = 125$, and the estimation sensor row $\boldsymbol{C}_2$ is placed at $x = 75$. The effect of the controller is quantified by $\boldsymbol{C}_1$, defined in a region spanned by 10 proper orthogonal decomposition (POD) modes (here indicated with a darker grey region); for each case, one set of modes is generated. In both cases, all the estimation sensors are connected to all the actuators (centralized control).

and 4 configurations for the streaks. The paper ends with a discussion in § 8 and a summary of the main conclusions (§ 9).

2. Governing equations and flow parameters

We study the dynamics and control of small-amplitude perturbations in a viscous, incompressible flow over a flat plate, using numerical simulations. The 3D input–output configuration, shown in figure 1, is an extension of the 2D case studied in Bagheri *et al.* (2009*a*,*b*). The disturbance velocity field is governed by the

Navier–Stokes equations linearized around a spatially evolving zero-pressure-gradient boundary-layer flow $\boldsymbol{u}(\boldsymbol{x}, t) = (U(x, y), V(x, y), 0)^{\mathrm{T}}$,

$$\frac{\partial \boldsymbol{u}}{\partial t} = -(\boldsymbol{U}\cdot\nabla)\,\boldsymbol{u} - (\boldsymbol{u}\cdot\nabla)\,\boldsymbol{U} - \nabla p + Re^{-1}\nabla^2\boldsymbol{u} + \lambda_f(x)\boldsymbol{u}, \tag{2.1a}$$

$$0 = \nabla\cdot\boldsymbol{u}, \tag{2.1b}$$

$$\boldsymbol{u} = \boldsymbol{u}_0, \quad \text{at } t = 0. \tag{2.1c}$$

The disturbance velocity field and the pressure field are $\boldsymbol{u}(\boldsymbol{x}, t) = (u, v, w)^{\mathrm{T}}$ and $p(\boldsymbol{x}, t)$, respectively. The flow evolves in the spatial domain Ω defined by

$$\Omega = \{\boldsymbol{x} \in \mathbb{R}^3 | x \in [0, L_x],\, y \in [0, L_y],\, z \in [-L_z/2, L_z/2]\}, \tag{2.2}$$

where the streamwise, wall-normal and spanwise directions are denoted by x, y and z, respectively. The Reynolds number is defined as $Re = U_\infty \delta_0^*/\nu$, where δ_0^* is the displacement thickness at the inflow position, U_∞ is the uniform free-stream velocity and ν is the kinematic viscosity. The simulations were performed at $Re_{\delta_0^*} = 1000$, corresponding to $Re_x \approx 3 \times 10^5$ at the computational inlet.

The following boundary conditions are imposed in Ω:

$$\boldsymbol{u}(x, y, -L_z/2) = \boldsymbol{u}(x, y, L_z/2), \tag{2.3a}$$

$$\boldsymbol{u}(0, y, z) = \boldsymbol{u}(L_x, y, z), \tag{2.3b}$$

$$\boldsymbol{u}(x, 0, z) = \boldsymbol{u}(x, L_y, z) = 0. \tag{2.3c}$$

A no-slip condition is imposed on the flat plate ($y = 0$). Far away from the wall ($y = L_y$), in the free stream, Dirichlet boundary conditions enforce vanishing perturbations. Periodicity of the solution is assumed in the spanwise direction, whereas in the streamwise direction, an outflow boundary condition is imposed within the Fourier approximation by the term $\lambda_f(x)\boldsymbol{u}$ in (2.1a). This forcing is identically zero inside the physically relevant domain ($x \in [0, 800]$) and rises to order one inside a fringe region, starting at $x = 800$, where it forces the perturbations to zero (Nordström, Nordin & Henningson 1999).

In this work, our aim is to present the linear systems and control theory in as simple and compact form as possible and put the focus on the control performance and the associated physics. Therefore, we omit entirely any discussion of partial differential equations (PDEs) and the following analysis is presented for finite-dimensional systems – ordinary differential equations (ODEs) – for simplicity. The infinite-dimensional formulation of the theory is presented in Bagheri *et al.* (2009*b*), where the relevant function spaces, inner products and derivations of adjoint operators alongside a more in-depth theoretical discussion are provided. Note, however, that the fundamental difference between the theory for ODEs and PDEs is related to convergence (see e.g. Curtain & Zwart 1995); other than that, the two formulations are analogous.

The results presented in this paper are computed with a pseudo-spectral code (Chevalier *et al.* 2007*b*). The computational domain Ω has the dimensions indicated in the captions of tables 1 and 2; a resolution of $768 \times 101 \times 120$ has been deemed sufficient and used for all the simulations. The spatial discretization requires thus $n \approx 10^7$ degrees of freedom. The discretized and linearized Navier–Stokes equations (2.1) with the boundary conditions (2.3) can be written as an initial-value problem as

$$\dot{\boldsymbol{u}}(t) = \boldsymbol{A}\boldsymbol{u}(t), \quad \boldsymbol{u}(0) = \boldsymbol{u}_0, \tag{2.4}$$

where $\boldsymbol{u} \in \mathbb{U} \subset \mathbb{R}^n$ is the state variable in the state space $\mathbb{U}$ endowed with the inner product $\langle \cdot, \cdot \rangle_\Omega$. For the flat-plate boundary layer, the flow is globally stable (Åkervik *et al.* 2008) – but convectively unstable – resulting in a stable matrix $\boldsymbol{A}$, i.e. all the eigenvalues of $\boldsymbol{A}$ have negative real part.

The action of $\boldsymbol{A} \in \mathbb{R}^{n \times n}$ on $\boldsymbol{u}$ corresponds to evaluating the right-hand side of the linearized Navier–Stokes equations and enforcing the boundary conditions. Associated with this operator is the evolution operator $\boldsymbol{T}$, which can be defined as

$$\boldsymbol{u}(t) = \boldsymbol{T}(t)\boldsymbol{u}(0) = \exp(\boldsymbol{A}t)\boldsymbol{u}_0. \tag{2.5}$$

Given an initial flow field $\boldsymbol{u}_0$, $\boldsymbol{T}$ provides the velocity field at a later time t; the action of the operator amounts to integrating the governing equations forward in time. In a similar way, the adjoint evolution operator $\boldsymbol{T}^*$ provides the solution of the adjoint linearized Navier–Stokes equations at different instants in time. Applying this operator corresponds to integrating the adjoint state backwards in time. The continuous and discrete adjoint equations are given in Appendix A; a detailed derivation of the operators for the corresponding two-dimensional case is provided in Bagheri *et al.* (2009*b*).

3. Input–output system and model reduction

The input–output configuration is schematically depicted in figure 1; formally, the linear system with inputs and outputs is defined as follows:

$$\dot{\boldsymbol{u}}(t) = \boldsymbol{A}\boldsymbol{u}(t) + \boldsymbol{B}_1\boldsymbol{w}(t) + \boldsymbol{B}_2\boldsymbol{\phi}(t), \tag{3.1a}$$

$$\boldsymbol{z}(t) = \boldsymbol{C}_1\boldsymbol{u}(t) + \boldsymbol{I}_l\boldsymbol{\phi}(t), \tag{3.1b}$$

$$\boldsymbol{v}(t) = \boldsymbol{C}_2\boldsymbol{u}(t) + I_\alpha\boldsymbol{g}(t). \tag{3.1c}$$

The first input $\boldsymbol{B}_1 \in \mathbb{R}^n$, located far upstream, models an incoming external perturbation, whereas the second input $\boldsymbol{B}_2 \in \mathbb{R}^{n \times m}$ represents m actuators. The temporal behaviour of the inputs is given by the signals $\boldsymbol{w} \in \mathbb{R}$, $\boldsymbol{g} \in \mathbb{R}$ and $\boldsymbol{\phi} \in \mathbb{R}^m$ respectively. The measurement signals, contained in the vectors $\boldsymbol{v} \in \mathbb{R}^p$ and $\boldsymbol{z} \in \mathbb{R}^k$, provide information about the perturbation and are extracted by p sensors $\boldsymbol{C}_2 \in \mathbb{R}^{p \times n}$ and k sensors $\boldsymbol{C}_1 \in \mathbb{R}^{k \times n}$, respectively. To model measurement noise corrupting the sensors signals, the output equation (3.1*b*) is forced with unit-variance white noise $\boldsymbol{g}(t)$. The vector $I_\alpha \in \mathbb{R}^p$ contains in each entry the scalar value α. A large value of α introduces a high level of noise corruption on the measurement $\boldsymbol{v}(t)$, whereas a small value indicates high fidelity of the information extracted by the sensors $\boldsymbol{C}_2$. Finally, the matrix $I_l \in \mathbb{R}^{k \times m}$ contains in each entry the parameter l, which allows penalization of the controller effort, as further discussed in § 3.3.

The energy growth of the TS wavepacket and the streaks is characterized by different growth rates and temporal scales: whereas the TS wavepacket grows at an exponential rate and breaks down quite far downstream of the inflow, the streaks grow at an algebraic rate, quickly reaching the maximum level of energy and resulting in a relatively early breakdown. The different time scales of the disturbances have vital implications for the control design as shown in figure 1; in order to mitigate properly the two types of disturbances, a proper control scheme for each case is designed. The set-up designed for the mitigation of the streaks is located upstream in the domain, before the maximum growth is reached. Conversely, the location of the TS wavepacket controller is chosen in the centre of the box, since the maximum

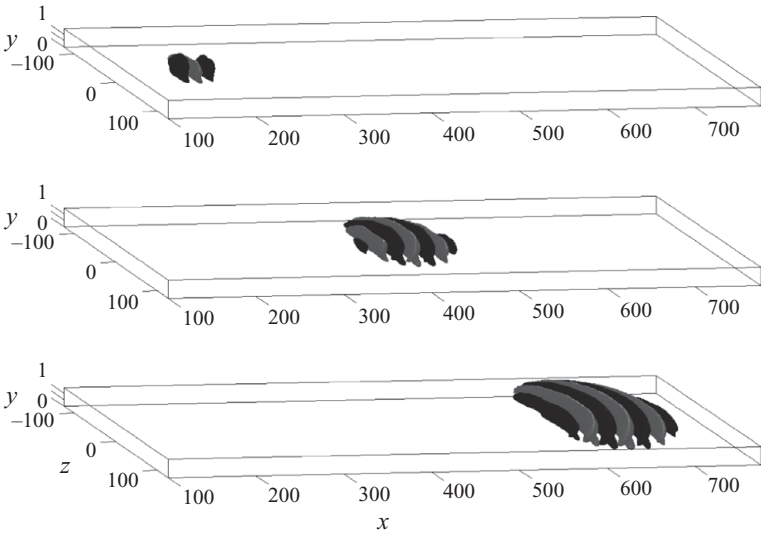

FIGURE 2. Impulse response of the system to an initial disturbance in $\boldsymbol{B}_1$, leading to maximum energy growth at time $T = 1820$; the streamwise component of the resulting disturbance is displayed at $t = 400$, 800 and 1600. The lighter and darker grey represent positive and negative velocities, respectively. The spreading of a TS wavepacket is observed.

growth appears far downstream. In the following sections, the $m+1$ inputs and $p+k$ outputs are introduced in detail.

3.1. $\boldsymbol{B}_1$: *optimal disturbances*

The upstream disturbance $\boldsymbol{B}_1$ is a localized initial condition that provides the maximum energy of the perturbation at a given final time. As recently shown by Monokrousos *et al.* (2010*a*), different instability mechanisms can be triggered by three-dimensional, localized initial conditions computed for different optimization times. In particular, long optimization time provides an initial condition that triggers a wavepacket of TS waves, whereas streamwise vortices are obtained as an optimal initial condition when large amplification in short time is sought.

Figure 2 shows the impulse response to an initial condition $\boldsymbol{B}_1$ that provides the maximum growth for a final time $t_{max} \approx 1820$ at three instants in time; the streamwise component is tilted in the upstream direction, leaning against the shear layer. Initially, the evolving disturbance extracts energy from the mean flow via the Orr mechanism (see e.g. Butler & Farrell 1992; Åkervik *et al.* 2008); the structure gradually rotates until it aligns with the shear. As the disturbance propagates downstream, the wavepacket grows in size and spreads in the spanwise direction. The evolution of the disturbance energy, defined as

$$E(t) = \langle \boldsymbol{u}(t), \boldsymbol{u}(t) \rangle_{\Omega}, \tag{3.2}$$

is shown in figure 4(*a*). We observe an exponential growth of the energy and an amplification $E(t_{max})/E(0) \approx 2 \times 10^3$.

The evolution of the optimal initial condition obtained for a shorter time, $t_{max} = 720$, is depicted in figure 3. The initial condition is a packet of streamwise vortices, with most of the energy contained in the wall-normal and spanwise components. The energy growth is related to the lift-up mechanism, characterized by the energy transfer to the streamwise component; this instability mechanism generates long streaky structures,

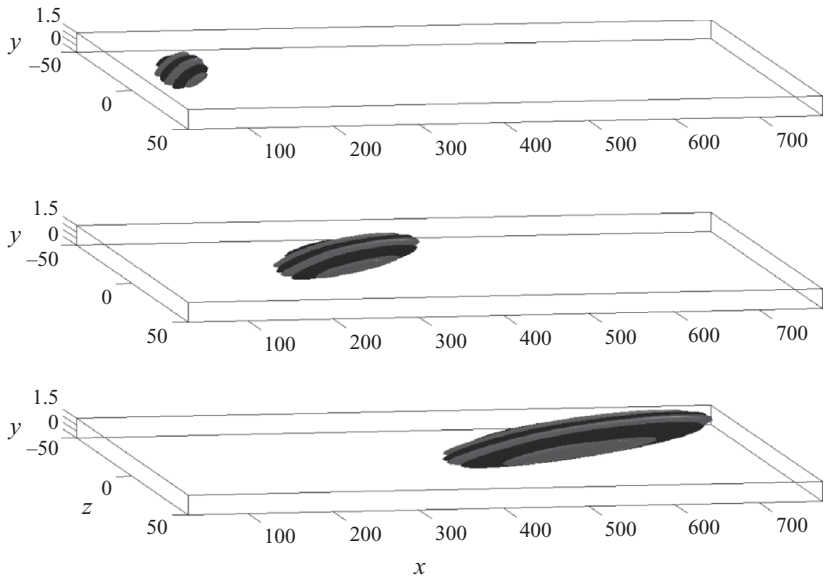

FIGURE 3. Impulse response to an optimal initial disturbance in $\boldsymbol{B}_1$ leading to maximum energy growth at $T = 720$. The disturbances are represented by the isosurfaces of the streamwise velocity at $t = 100, 400$ and 800; the lighter and darker grey represent positive and negative velocity, respectively. The resulting disturbance is characterized by elongated streaky structures.

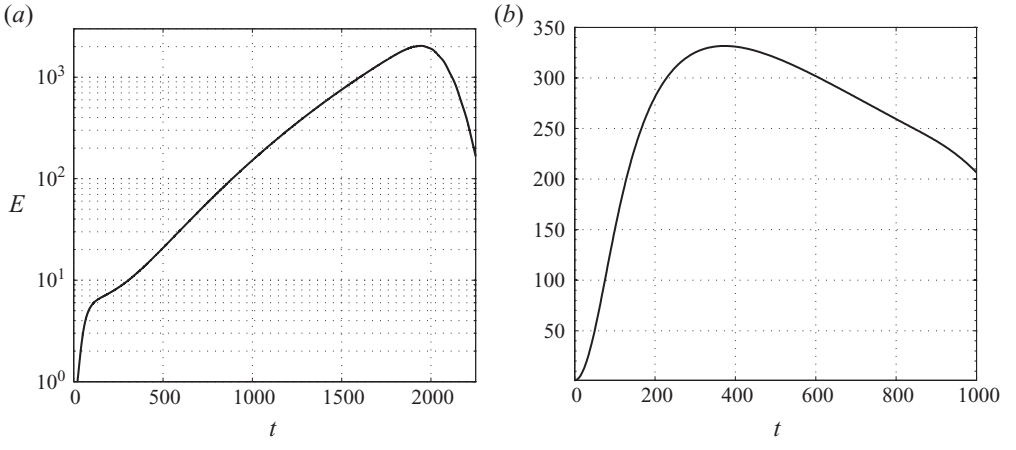

FIGURE 4. Disturbance energy as a function of time for the TS waves (*a*) and streaks (*b*).

growing in size in the streamwise direction, as shown in figure 3. The energy evolution is shown in figure 4(*b*), where an amplification $E(t_{max})/E(0) \approx 3 \times 10^2$ is found.

3.2. $\boldsymbol{B}_2$ *and* $\boldsymbol{C}_2$*: actuators and sensors*

Each of the m actuators in $\boldsymbol{B}_2$ is represented by a volume forcing localized in a region close to the wall. The actuators are placed in a row in the spanwise direction; the p sensors represented by $\boldsymbol{C}_2$ are also composed of a row of localized elements, located a short distance upstream of the actuators. All the elements in $\boldsymbol{B}_2$ and $\boldsymbol{C}_2$ are analytically expressed by a Gaussian function given in Appendix B. The fact that we have modelled the actuators and sensors as volume forcing does not mean that

they are unrealistic or not relevant for practical implementation; it is the effect of an actuator that is important to model, and not the actuator itself. Therefore, the action that the volume forcing has on the flow could possibly be reproduced, for example using plasma actuators (Grundmann & Tropea 2008). The measurement signal $\boldsymbol{v}(t)$ is the spatial integral of the velocity field $\boldsymbol{u}$ weighted with the Gaussian function (see (B 3)).

The actuator array designed for the mitigation of the TS wavepackets is located halfway in the downstream direction, while the array designed for the streaks control is placed upstream; it was found by numerical simulations that the performance of the feedback control schemes is dependent on the number of elements used and the streamwise location, as discussed later.

3.3. $\boldsymbol{C}_1$: *objective function*

The aim is to determine a control signal $\phi(t)$ using the noisy measurements $\boldsymbol{v}(t)$, so that the perturbation energy of the flow is minimized in the region defined by $\boldsymbol{C}_1$. Moreover, the energy expended by the actuator has to be limited in order to design an efficient controller. Hence, the criterion to be minimized is expressed by the objective function

$$\|\boldsymbol{z}\|^2_{L^2(0,T)} = \int_0^T \|\boldsymbol{C}_1\boldsymbol{u}\|^2_{\Omega} + \phi^T \boldsymbol{I}_l^T \boldsymbol{I}_l \phi \, \mathrm{d}t, \tag{3.3}$$

where the entries of the matrix $\boldsymbol{I}_l$, given by the parameter l, define the cost of the control; note that we assumed the cross-term between the control input and $\boldsymbol{C}_1\boldsymbol{u}$ to be zero (Zhou, Doyle & Glover 2002). Low values of l allow strong actuations, as the control input is allowed to have a higher magnitude. On the other hand, high values of l penalize strong actutation. Also, it is worth noting that values of l that are too low may result in unphysical control inputs.

The spatial support for $\boldsymbol{C}_1$ is localized in a region downstream, where disturbances have high energy, as sketched in figure 1. The subspace of the domain where the controller minimizes the energy is spanned by a basis $\{\boldsymbol{C}_{1,1}, \ldots, \boldsymbol{C}_{1,k}\}$, which in the present configurations is a sequence of POD modes (see e.g. Holmes, Lumley & Berkooz 1996), obtained from the impulse response of the initial disturbances. This approach is similar to the so-called output projection technique used by Rowley (2005) and Ilak & Rowley (2008). The POD modes are the most energetic structures triggered by the inputs; the corresponding eigenvalues $\{\gamma_1 \geqslant \gamma_2 \geqslant \cdots \geqslant \gamma_k\}$ represent the fraction of the total flow energy captured by each mode.

The POD basis is empirical, i.e. it accurately represents the data that generated it; therefore, two different sets of modes are computed, one for each initial condition considered. The POD modes generated for the TS wavepacket configuration come in pairs (see e.g. Rempfer & Fasel 1994), because two real-valued functions are required to describe a flow structure travelling as a wavepacket; each pair exhibits the same structure, only shifted in the streamwise direction. In contrast, the corresponding POD eigenvalues associated with the streak disturbance, not shown here, are no longer ordered in pairs, since the disturbance is characterized by low-frequency elongated structures in the direction of propagation.

To identify a proper POD basis, we also considered snapshots generated from all the inputs (i.e. including the actuators). The comparison between the POD modes generated by all the inputs ($\boldsymbol{B}_1$ and $\boldsymbol{B}_2$) and those obtained from the initial condition ($\boldsymbol{B}_1$) demonstrated that only modes corresponding to small γ, containing less than 1 % of the total energy, are affected by the structures related to the actuators. Thus, POD modes generated only by the upstream disturbance were used during the numerical

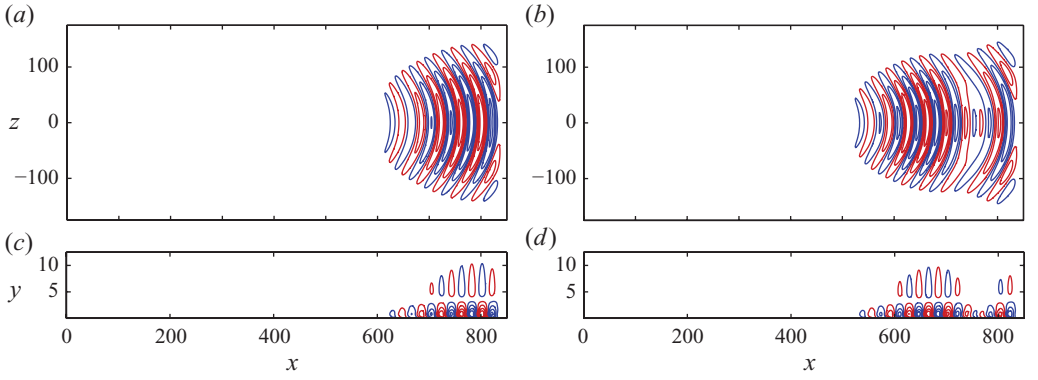

FIGURE 5. POD modes generated from the impulse response to an initial condition triggering TS waves. The isocontours of the streamwise velocity component of the first mode ($\boldsymbol{C}_{1,1}$) are shown in the xz-plane at $y \approx 1.0$ (a) and in the xy-plane at $z = 0$ (c); red contours indicate positive velocity, blue contours the negative one. Analogously, the third POD mode ($\boldsymbol{C}_{1,3}$) is shown in (b, d).

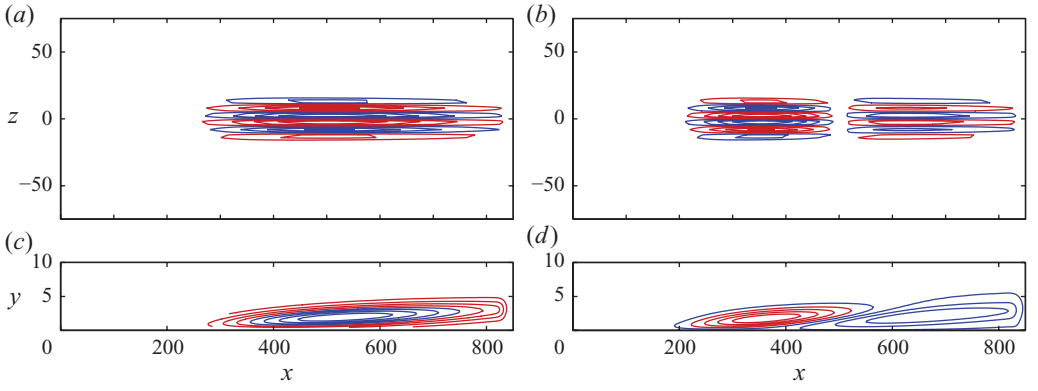

FIGURE 6. POD modes generated from the impulse response to an initial condition triggering streaks. The isocontours of the streamwise velocity component of (a, c) the first ($\boldsymbol{C}_{1,1}$) and (b, d) second ($\boldsymbol{C}_{1,2}$) POD modes; the sections in the xz-plane, at $y \approx 1.6$, are shown in (a) and (b), whereas the sections in the xy-plane, at $z = 2$, are shown in (c) and (d). Red contours indicate positive velocity and blue contours indicate negative velocity.

simulation; in particular, the first 10 POD modes capture 93 % and 91 % of the total flow energy for the TS and streak configurations, respectively, and are used as the basis for C_1. An alternative choice for $\boldsymbol{C}_1$ is presented in Semeraro *et al.* (2010), where a set of Fourier modes localized in the streamwise and wall-normal directions were introduced to define the objective function.

The leading POD modes capture the relevant spatial characteristics of each disturbance as illustrated in figures 5 and 6, where two modes for each set are shown. For the TS wavepacket (figure 5), one POD mode for each of the two first pairs is shown: it can be seen that the structure is mostly located downstream, indicating where the energy response to the forcing is the largest. For the streaks (figure 6), the first two modes have significant spatial support starting from $x = 250$ and extend all the way to the end of the domain. The streamwise and the wall-normal components are antisymmetric with the respect to the xy-plane ($z = 0$), whereas the

spanwise component is symmetric; opposite symmetry features are observed for the TS wavepackets. The cross-section reveals the tilted shape of the modes, with the streak leading edge further away from the wall than the trailing edge.

3.4. *Model reduction*

In general, a reduced-order model of the input–output system (3.1) can be obtained via a projection onto a low-dimensional subspace $\mathbb{U}_r \subset \mathbb{U}$, spanned by r basis functions, $\boldsymbol{\Phi} = (\boldsymbol{\phi}_1, \boldsymbol{\phi}_2, \ldots, \boldsymbol{\phi}_r) \in \mathbb{R}^{n\times r}$. Thus, the disturbance field $\boldsymbol{u} \in \mathbb{U}$ can be approximated by $\tilde{\boldsymbol{u}} \in \mathbb{U}_r$,

$$\tilde{\boldsymbol{u}} = \sum_{j=1}^{r} q_j \boldsymbol{\phi}_j = \boldsymbol{\Phi} q, \tag{3.4}$$

where $q = (q_1, q_2, \ldots, q_r)^{\mathrm{T}} \in \mathbb{R}^r$ are the scalar expansion coefficients. The coefficients can be computed from

$$q_j = \langle \boldsymbol{u}, \boldsymbol{\psi}_j \rangle_\Omega \quad \text{or } q = \boldsymbol{\Psi}^* \boldsymbol{u}, \tag{3.5}$$

where $\boldsymbol{\Psi} = (\boldsymbol{\psi}_1, \boldsymbol{\psi}_2, \ldots, \boldsymbol{\psi}_r) \in \mathbb{R}^{n\times r}$ are adjoint modes; the adjoint modes are bi-orthogonal to the expansion basis $\boldsymbol{\Phi}$, i.e. $\boldsymbol{\Psi}^* \boldsymbol{\Phi} = \boldsymbol{I}$, where $\boldsymbol{I} \in \mathbb{R}^{r\times r}$ is the identity matrix. The asterisk represents the application of the inner product $\langle \cdot, \cdot \rangle_\Omega$ between the rows of $\boldsymbol{\Psi}^*$ and $\boldsymbol{u}$. The approximation (3.4) can be inserted in the input–output system (3.1). Taking the inner product with the adjoint modes results in the reduced-order model of order r,

$$\dot{q}(t) = \boldsymbol{A}_r q(t) + \boldsymbol{B}_{1r} \boldsymbol{w}(t) + \boldsymbol{B}_{2r} \phi(t), \tag{3.6a}$$

$$\boldsymbol{z}(t) = \boldsymbol{C}_{1r} q(t) + \boldsymbol{I}_l \phi(t), \tag{3.6b}$$

$$\boldsymbol{v}(t) = \boldsymbol{C}_{2r} q(t) + I_\alpha \boldsymbol{g}(t), \tag{3.6c}$$

where $\boldsymbol{A}_r = \boldsymbol{\Psi}^* \boldsymbol{A} \boldsymbol{\Phi}$, $\boldsymbol{B}_{1r} = \boldsymbol{\Psi}^* \boldsymbol{B}_1$, $\boldsymbol{B}_{2r} = \boldsymbol{\Psi}^* \boldsymbol{B}_2$, $\boldsymbol{C}_{1r} = \boldsymbol{C}_1 \boldsymbol{\Phi}$ and $\boldsymbol{C}_{2r} = \boldsymbol{C}_2 \boldsymbol{\Phi}$.

The choice of a proper expansion basis is crucial for the performance of the reduced-order model; in our case, we aim to build a model that preserves the dynamics between the actuators and sensors. Indeed, among all the possible divergence-free velocity fields, only certain states can be triggered by the inputs ($\boldsymbol{B}_1$ and $\boldsymbol{B}_2$) and observed by the outputs ($\boldsymbol{C}_1$ and $\boldsymbol{C}_2$). These states are called *controllable* and *observable* states, respectively. The unobservable/uncontrollable states are redundant for the input–output behaviour of the system; thus, they can be discarded. Moreover, it turns out that, when $m, p \ll n$, with m being the number of inputs and p the number of the outputs, the complexity of (3.1) can be further reduced, while preserving the relation between the inputs and outputs.

A systematic approach of removing these states is called *balanced truncation* (Moore 1981); in Appendix C a summary of this method is given in a simplified space-discrete form. The focus is on the Hankel operator, which provides a direct mapping between the inputs and the outputs. From this operator, a set of *balanced modes* and a corresponding adjoint set can be defined, and used as a projection basis. Unfortunately, the necessity to solve Lyapunov equations makes the exact balanced truncation unfeasible for large systems. An approximation based on snapshots of the flow field is introduced in Rowley (2005). In particular, the snapshots are computed by marching in time the linearized NS forced by all inputs, and backward in time the adjoint system forced by the sensors. In Appendix C, the method is briefly outlined for the present notation; note, however, that the original method proposed by Rowley (2005), also referred to as balanced proper orthogonal decomposition (BPOD), is

characterized by the *output projection* of the sensor over a POD basis generated from the inputs data set.

Further extensions of balanced truncation are available for unstable systems and nonlinear problems. Indeed, a balanced truncation as introduced by Moore (1981) can be applied only to a system linearized about a stable steady state. An extension to unstable cases was proposed by Zhou, Salomon & Wu (1999); the method relies on the identification of the stable and the unstable states, for instance via a modal decomposition, and the application of balancing to those subspaces. Recently, the method was applied using the snapshot-based approximation for the control of unstable flows such as the open cavity case (Barbagallo, Sipp & Schmid 2009) or the flow past a flat plate (Ahuja & Rowley 2010); in those cases, the unstable dynamics of the system is represented by the unstable modes, while the approximate balance truncation is applied to obtain a reduced-order model of the stable partition of the system. Finally, an interesting application to nonlinear systems is presented in Ilak *et al.* (2010), where reduced-order models for the complex Ginzburg–Landau equation are compared. The best performance is obtained by Galerkin projection of the nonlinear system onto a basis of balanced modes obtained from the corresponding linearized system.

4. Reduced-order models

In this section, we discuss the set of approximate balanced modes – and the related adjoint set – computed for both the TS and streak cases. The structure of the modes is investigated, pointing out the main structural features. Indeed, an advantage of this technique is the possibility of analysing the spatial distribution of the modes; the spatial support reveals peculiarities of the flow from the input–output point of view and provides physical insight into the sensors/actuators placement. In fact, the resulting balanced mode $\boldsymbol{\phi}_j$ is the global structure in the flow that is 'influenced' by the input $\boldsymbol{B}$ by an amount given by its Hankel singular value (HSV) – see Appendix C. The corresponding adjoint mode $\boldsymbol{\psi}_j$ is a flow structure that – if used as an initial condition – will result in an output energy given also by its HSV. Thus, these global modes represent flow fields ranked according to their response behaviour (controllability) and output sensitivity (observability).

In this section, we first discuss the balanced modes obtained by considering only the upstream disturbance $\boldsymbol{B}_1 \in \mathbb{R}^n$ and the outputs $\boldsymbol{C}_1 \in \mathbb{R}^{k\times n}$ (POD modes), for the sake of clarity. Finally, the reduced-order models for the full system, including also the actuators $\boldsymbol{B}_2 \in \mathbb{R}^{n\times m}$ and sensors $\boldsymbol{C}_2 \in \mathbb{R}^{p\times n}$, are presented and their performance is analysed. One model is computed for each configuration; in table 1, 11 different configurations (labelled A–M) for the TS mitigation are listed. In all cases, the elements have an equidistant spacing in the spanwise direction at $\Delta_z = 20$. The relative position of the arrays in the streamwise direction is fixed; the distance among the actuators was chosen after preliminary tests to get a proper actuation. For the streaks, we found that a finer distribution, $\Delta_z = 4$, of the actuator elements in the spanwise direction is necessary. This is mainly due to the smaller spanwise scales of the streaks ($\beta = 2\pi/L_z = 0.58$, with a total width of $L_z \approx 11$). In table 2, the configurations for the control of streaks are listed, labelled N–Q. For the largest cases, the linear systems consist of 10 inputs and 19 outputs (case A, table 1), and 9 inputs and 18 outputs (case N, table 2); their complexity n is of the order of 10 million.

The TS case and the streaks are discussed separately in the following sections.

Case	Actuators m	Sensors p	Control penalty l	Noise corruption α	Energy reduction E/E_{nc}	System norm $\|\boldsymbol{G}\|_2^2$
Ts0	–	–	–	–	1.00	324.25
A	9	9	100	0.01	0.070	1.42
B	9	9	250	0.01	0.064	13.23
C	9	9	500	0.01	0.12	55.27
D	9	9	100	10	0.068	1.48
E	9	9	100	50	0.061	8.46
F	9	9	100	150	0.57	209.03
G	9	9	100	250	0.85	318.74
H	3	3	100	0.01	0.55	6.91
I	5	5	100	0.01	0.13	2.25
L	7	7	100	0.01	0.071	1.28
M	9	5	100	0.01	0.068	1.56

TABLE 1. Cases A–M correspond to 11 closed-loop systems for the control of TS wavepacket, whereas case 'Ts0' is an uncontrolled configuration. In all the cases, the computational box Ω has dimensions $[L_x, L_y, L_z] = (100, 30, 120\pi)$. The number of actuators $\boldsymbol{B}_2$ (m), the number of sensors $\boldsymbol{C}_2$ (p), the control penalty (l) and the degree of noise corruption (α) vary for the different configurations. The peak perturbation energy of the controlled cases as a fraction of the uncontrolled peak disturbance energy, together with the 2-norm of the input–output system transfer function, is also displayed.

Case	Actuators m	Sensors p	Control penalty l	Energy reduction E/E_{nc}	System norm $\|\boldsymbol{G}\|_2^2$
Sk0	–	–	–	1.00	114.24
N	8	8	50	0.66	38.84
O	8	8	100	0.67	79.85
P	8	8	150	0.81	96.40
Q	8	8	70	0.79	55.96

TABLE 2. Cases N–Q correspond to four closed-loop systems for the control of streaks, whereas case 'Sk0' is an uncontrolled configuration. The control penalty (l) varies for the different configurations; the measurement noise is $\alpha = 0.01$ for all set-ups. The same number (m) of actuators $\boldsymbol{B}_2$ (m) and sensors $\boldsymbol{C}_2$ (p) is considered for all the configurations; in the last configuration, a different layout is considered, where the sensor array and the actuator array are placed in $x = 100$ and $x = 150$, respectively. The dimensions of the computational domain for all the cases are $[L_x, L_y, L_z] = (1000, 30, 240)$. The peak perturbation energy of the controlled cases as a fraction of the uncontrolled peak disturbance and the 2-norm is reported.

4.1. *TS wavepackets*

Using the snapshot method, the balanced modes and the adjoint balanced modes related to the TS wavepacket were computed; the snapshots were collected with constant time spacing, $\Delta t = 16$, in a time interval [0, 3000] for the forward simulation and in [0, −2600] for the 10 adjoint simulations.

The computed Hankel singular values σ_j are shown in figure 7 (circles). Similar to the POD modes discussed previously, the HSVs generated for the TS come in pairs, where the corresponding modes have the same structure, only shifted along the streamwise direction by a quarter of wavelength. The isocontours of the streamwise components of the first and the third balanced modes $(\boldsymbol{\phi}_1, \boldsymbol{\phi}_3)$ and their related adjoint modes $(\boldsymbol{\psi}_1, \boldsymbol{\psi}_3)$ are shown in figure 8; the structure is shown in both the xy-plane

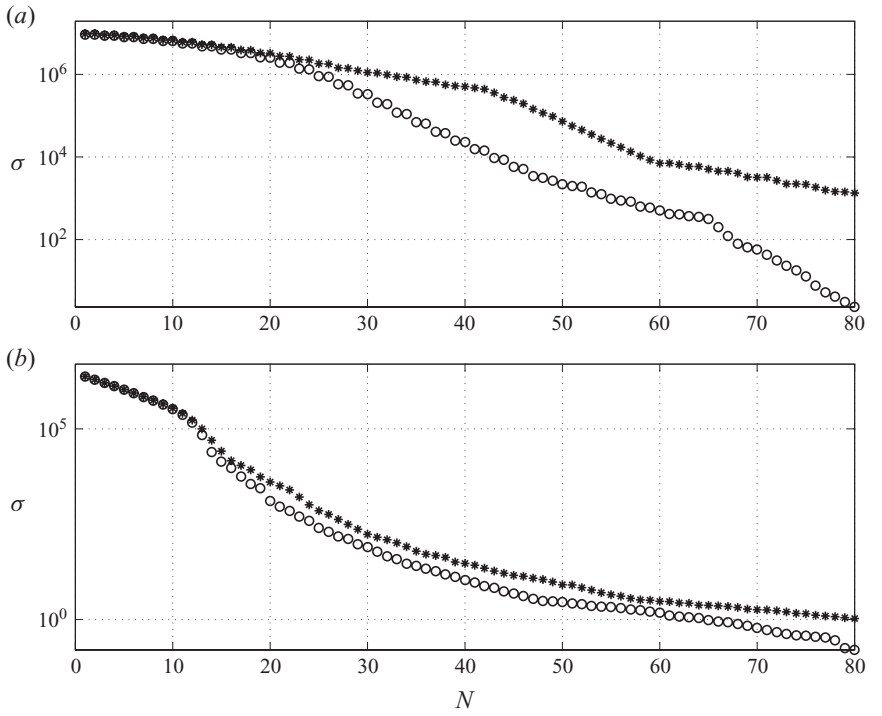

FIGURE 7. The Hankel singular values of the complete models (stars) are compared with the HSVs generated considering the first input $\boldsymbol{B}_1$ and the output $\boldsymbol{C}_1$ only (circles). On top Hankel singular values generated for the models related to TS waves (*a*), on bottom HSVs for the streaks (*b*).

($z=0$) and the xz-plane ($y\approx 1.6$). The leading balanced modes are characterized by a nearly two-dimensional TS wavepacket structure, located mostly in the downstream region. These modes are strongly controllable flow structures and capture the response behaviour of the system to the input $\boldsymbol{B}_1$.

The associated adjoint balanced modes are mostly located far upstream and represent flow structures to which the output $\boldsymbol{C}_1$ is most sensitive. The spatial separation between these structures and the most controllable structures identified by the direct balanced modes is similar to the spatial separation observed between the direct and adjoint global modes of the linearized Navier–Stokes equations, $\boldsymbol{A}$. This is a sign of the streamwise non-normality of $\boldsymbol{A}$ (Chomaz 2005). In figure 8(*b–d*), the streamwise component of the modes in the xy-plane ($z=0$) is shown. Here one can see a tilted structure leaning against the shear, similar to the optimal initial condition discussed in § 3.1.

Figure 7 shows the HSVs corresponding to the balanced modes used to compute the reduced-order model using all the inputs ($m+1$) and outputs ($p+k$) (stars), pertaining to case A in table 1. It is interesting to note that the associated HSVs decay slower than the HSVs computed using only $\boldsymbol{B}_1$ and $\boldsymbol{C}_1$ (circles). The leading singular values of the two systems are equal, indicating that the input–output dynamics of the system is strongly influenced by the energy triggered by the input $\boldsymbol{B}_1$ and the observability characteristics of the functions chosen as output $\boldsymbol{C}_1$.

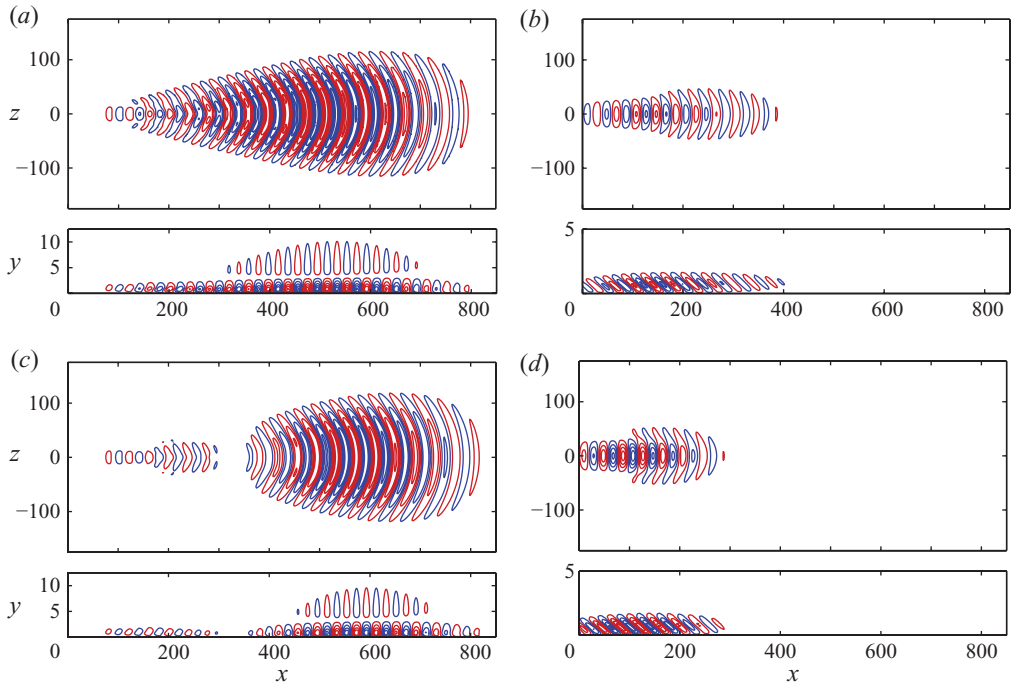

FIGURE 8. Balanced modes and related adjoint modes for the TS waves. Left: streamwise component of the leading balanced mode $\boldsymbol{\phi}_1$ (a) and the third balanced order mode $\boldsymbol{\phi}_3$ (c). Right: corresponding adjoint modes $\boldsymbol{\psi}_1$ (b) and $\boldsymbol{\psi}_3$ (d). Positive velocity is represented by red, while negative one is in blue; for all the modes depicted here, the top view is shown in the xz-plane at $y \approx 1.6$, the side view is in the section xy at $z = 0$.

One way to validate the snapshot-based balanced truncation is to check whether the controllability and observability Gramians of the reduced-order model are diagonal and equal to the HSVs. The diagonal elements of the Gramians associated with the reduced-order model and the HSVs were found to be the same for the first 80 modes. Owing to numerical discretization errors, higher-order modes gradually lose bi-orthogonality, causing the presence of off-diagonal elements in the Gramians.

To test the reduced-order model, we compare impulse responses of the Navier–Stokes system (3.1) with those obtained from the low-order model (3.6). For configuration A, there are in total 10 input signals and 19 output signals, resulting in 190 impulse responses. In figure 9, the following three signals are shown:

$$\boldsymbol{B}_1 \rightarrow \boldsymbol{C}_{2,0}, \quad \boldsymbol{B}_{2,0} \rightarrow \boldsymbol{C}_{1,1}, \quad \boldsymbol{B}_1 \rightarrow \boldsymbol{C}_{1,1}. \tag{4.1}$$

The second subscript of $\boldsymbol{B}_2$ and $\boldsymbol{C}_2$ indicates the element according to figure 1. In all the figures, the impulse responses of a reduced model of order $r = 60$ are shown by black dots, while the solid grey line provides the direct numerical simulation (DNS) results. We observe that the low-order model ($r = 60$) is able to preserve the input–output behaviour of the full Navier–Stokes system ($n \approx 10^7$), albeit the significant model-order reduction. The agreement between all the impulse responses of the two systems is as good as the three signals shown here.

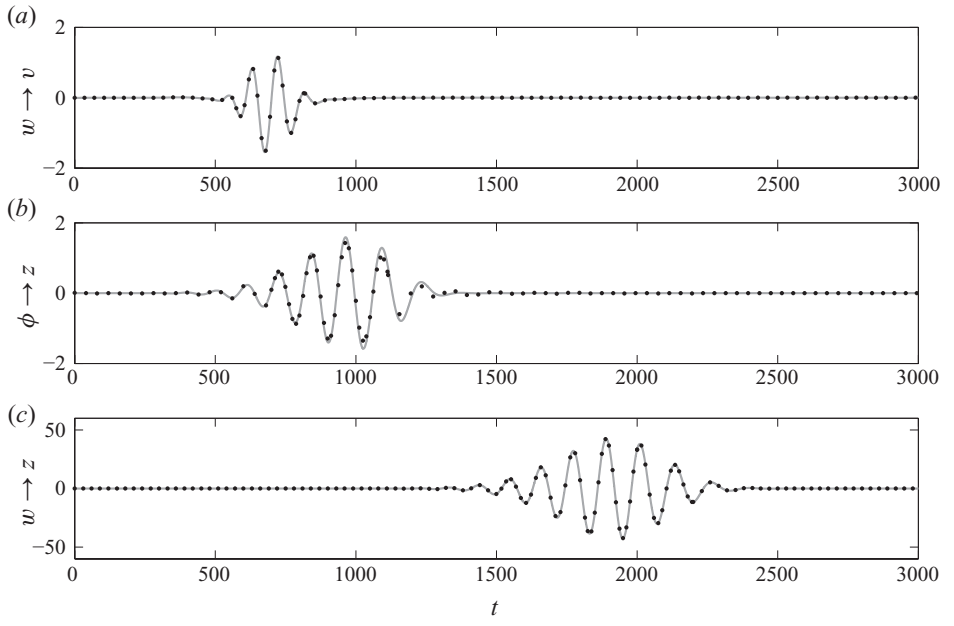

FIGURE 9. Impulse response of the system (a) from the input $\boldsymbol{B}_1$ to the output $\boldsymbol{C}_{2,0}$, (b) from $\boldsymbol{B}_{2,0}$ to $\boldsymbol{C}_{1,1}$ and (c) from $\boldsymbol{B}_1$ to $\boldsymbol{C}_{1,1}$, when a propagating TS wavepacket is considered. The grey line shows the DNS results, while the black dots indicate the impulse response of a reduced model of order 60.

4.2. *Streaks*

The approximate Hankel singular values generated for the streak case are shown in figure 7(b). In this case, the snapshots were collected with a constant time spacing, $\Delta t = 16$, in a time interval [0, 3000] for the forward simulation and a time interval [0, 2000] for the 10 adjoint simulations. In agreement with the POD results, the HSVs do not come in pairs, due to the low-frequency elongated structure characterizing the modes (see figure 10). The first two balanced modes resemble the POD modes depicted in figure 6 and show the typical structure aligned with the shear, in the xy section at $z \approx 3.1$. The streamwise velocity component u is one order of magnitude larger than v and w. The corresponding leading adjoint modes shown in figure 10(b, d) are located slightly more upstream and have an order of magnitude large value in v, w compared with u. Note that the spatial support of the balanced modes and the corresponding adjoint modes is nearly the same; the significant difference between the forward and adjoint modes is in the dominant velocity component. This is a sign of component-wise non-normality; the most efficient mechanism of growth of a streak is energy transfer from the wall-normal and spanwise components to the streamwise component.

As shown in figure 7(b) – similar to the case of the TS wavepacket – the HSVs of the complete system (including all inputs and outputs) decay slower than the HSVs computed using only $\boldsymbol{B}_1$ and $\boldsymbol{C}_1$ (stars) and the leading singular values of the two systems are equal.

A low-order model ($r = 60$) computed using balanced modes captures properly the input–output behaviour of the entire system ($n \approx 10^7$). The validation of the snapshot-based balanced truncation method and the properties of the reduced-order model were tested following the same steps as for the TS reduced-order model. In

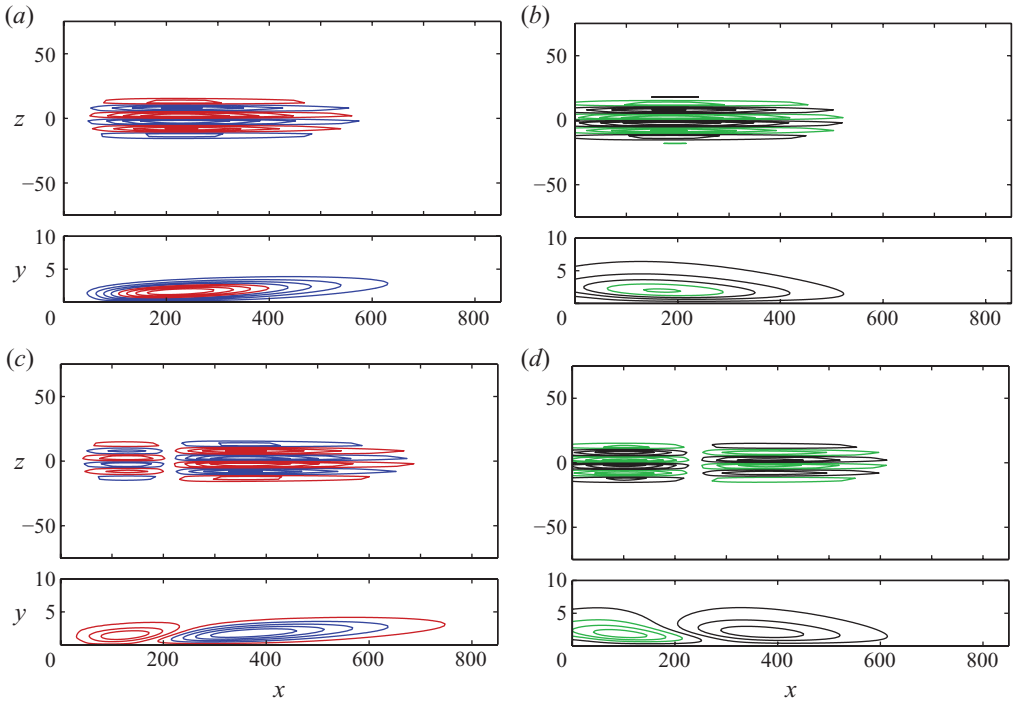

FIGURE 10. Leading balanced modes and related adjoint modes for the streaks. Left: streamwise component of the leading balanced mode $\boldsymbol{\phi}_1$ (a) and the second balanced order mode $\boldsymbol{\phi}_2$ (c). Positive velocity is represented by red, while negative one is in blue. Right: wall-normal component of the corresponding adjoint modes $\boldsymbol{\psi}_1$ (b) and $\boldsymbol{\psi}_2$ (d). Positive velocity is represented by black, while negative one is in green. For all the modes depicted here, the top view is shown in the xz-plane at $y \approx 1.6$, and the side view is in the section xy at $z = 2$.

figure 11, we compare the input–output behaviour of the full Navier–Stokes system and the reduced-order model, for the following three signals:

$$\boldsymbol{B}_1 \rightarrow \boldsymbol{C}_{2,-1}, \quad \boldsymbol{B}_{2,-1} \rightarrow \boldsymbol{C}_{1,1}, \quad \boldsymbol{B}_1 \rightarrow \boldsymbol{C}_{1,1}. \tag{4.2}$$

The second subscript of $\boldsymbol{B}_2$ and $\boldsymbol{C}_2$ indicates the element according to figure 1. A similar good agreement is observed for all the impulse responses, and we can conclude that input–output relation of the signals for the streak configuration can be adequately described with a low-dimensional model.

5. Feedback control

The aim of this section is to use the validated balanced reduced-order models to mitigate the growth of the disturbances. Although the steps taken to design the closed-loop control are the same as for the 2D case studied by Bagheri *et al.* (2009*b*), the control problem is significantly more complex due to the additional spanwise direction.

Since the reduced-order models show essentially the same input–output behaviour as the original system (but with only 60 degrees of freedom), they are used during the control design. Once the feedback controller is constructed, it can be applied on-line, in parallel to the DNS simulations.

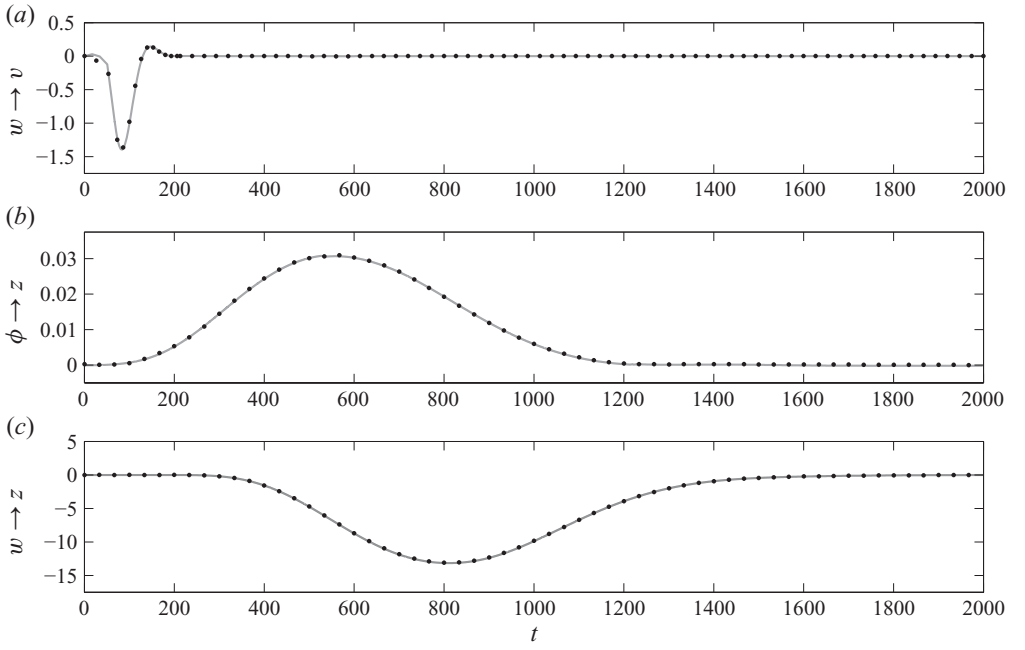

FIGURE 11. Impulse response of the system (*a*) from the input $\boldsymbol{B}_1$ to the output $\boldsymbol{C}_{2,-1}$, (*b*) from $\boldsymbol{B}_{2,-1}$ to $\boldsymbol{C}_{1,1}$ and (*c*) from $\boldsymbol{B}_1$ to $\boldsymbol{C}_{1,1}$ for the streak model. The grey line shows the DNS results, while the dotted black dots indicate the impulse response of a reduced model of order 60.

5.1. *Main steps of LQG design*

Using the tools of control theory, we can determine what action the actuators should take to minimize the disturbance energy in a region defined by $\boldsymbol{C}_1$, and if the action of an actuator should depend on all sensor measurements or only the sensor located upstream at the same spanwise location. In particular, the controller can be designed using the LQG approach. Assume that the external disturbance signal $\boldsymbol{w}(t)$ and the measurement noise $\boldsymbol{g}(t)$ in (3.6) are unit-variance white-noise processes. Then, based on the noisy measurements $\boldsymbol{v}(t)$ extracted from the sensors $\boldsymbol{C}_2$, the controller provides a control signal $\phi(t)$ for the actuators $\boldsymbol{B}_2$, such that the mean of the output energy of $\boldsymbol{z}$,

$$\mathscr{E}\left\{\|\boldsymbol{z}\|^2_{L^2[0,\infty)}\right\} = \mathscr{E}\left\{\int_0^\infty q^T \boldsymbol{C}_{1r}^T \boldsymbol{C}_{1r} q + \phi^T \boldsymbol{I}_l^T \boldsymbol{I}_l \phi \; \mathrm{d}t\right\}, \tag{5.1}$$

is minimized. The first step in constructing a controller is to estimate the full state $\boldsymbol{u}$ given only the noisy measurements $\boldsymbol{v}(t)$ – also referred to as the *estimation problem*. After the state has been successfully estimated, we assume, in a second step, that the control $\phi(t)$ and the estimated reduced state $\hat{q}(t) \in \mathbb{R}^r$ satisfy a linear relation involving some yet unknown matrix $\boldsymbol{K} \in \mathbb{R}^{m\times r}$, i.e.

$$\phi(t) = \boldsymbol{K}\hat{q}(t). \tag{5.2}$$

The goal of this second step is then to find such a matrix $\boldsymbol{K}$, which is referred to as the control gain. One attractive feature of the LQG design is that the two steps (estimation and full-information problem) can be performed independently of

each other, (see Anderson & Moore 1990). Moreover, if both problems are optimal and stable, the resulting closed-loop system, composed of the two problems, is also optimal and stable. The main disadvantage of LQG is that it does not account for uncertainties of the underlying system $(\boldsymbol{A}, \boldsymbol{B}, \boldsymbol{C})$ (see Doyle 1978). One can only check the robustness by *ad hoc* testing the controller for various parameters.

For a derivation of the LQG solution, please refer to e.g. Lewis & Syrmos (1995) and Bagheri *et al.* (2009*c*) for a 'classical' optimal control framework or Doyle *et al.* (1989) and Dullerud & Paganini (1999) for a more 'modern' robust control framework. Here, we just state the solution of the two separate problems.

To estimate the full state $\boldsymbol{u}(t)$ given only the noisy measurements $\boldsymbol{v}(t)$, an estimator that governs the dynamics of an estimated state $\hat{q}$ can be introduced:

$$\dot{\hat{q}}(t) = \boldsymbol{A}_r\hat{q}(t) + \boldsymbol{B}_{2r}\phi(t) + \boldsymbol{L}(\boldsymbol{v}(t) - \hat{\boldsymbol{v}}(t)). \tag{5.3}$$

In the above expression, we compare the measurement from the velocity field $\boldsymbol{v} = \boldsymbol{C}_2\boldsymbol{u}$ and the measurement from the estimated state $\hat{\boldsymbol{v}} = \boldsymbol{C}_{2r}\hat{q}$ and feed back the mismatch in these two quantities using the estimator gain $\boldsymbol{L} \in \mathbb{R}^{r\times p}$. It can be shown (Kalman 1960) that the estimation gain that minimizes the estimation error $\|q - \hat{q}\|$, and results in a stable system given by

$$\boldsymbol{L} = -\frac{1}{\alpha^2}\boldsymbol{Y}\boldsymbol{C}_{2r}^T, \tag{5.4}$$

where $\boldsymbol{Y} \in \mathbb{R}^{r\times r}$ is a solution to an algebraic Riccati equation (see e.g. Laub 1991).

In the second step, assume that the full state is given by q at all times and that $\phi(t) = \boldsymbol{K}q(t)$ (instead of (5.2)). Inserting the feedback relation into (3.1) and neglecting the output $\boldsymbol{v}$, we get

$$\dot{q}(t) = (\boldsymbol{A}_r + \boldsymbol{B}_{2r}\boldsymbol{K})q(t) + \boldsymbol{B}_{1r}\boldsymbol{w}(t), \tag{5.5a}$$

$$z(t) = \boldsymbol{C}_{1r}q(t) + \boldsymbol{I}_l\phi(t). \tag{5.5b}$$

It remains to choose $\boldsymbol{K} \in \mathbb{R}^{m\times r}$ such that the system is stable and the control signal $\phi(t)$ minimizes output energy, $\|z\|^2$. The solution is provided by an optimal control state-feedback problem (see e.g. Anderson & Moore 1990), where the optimal control signal is given by

$$\boldsymbol{K} = -\tfrac{1}{2}\left(\boldsymbol{I}_l^T\boldsymbol{I}_l\right)^{-1}\boldsymbol{B}_{2r}^T\boldsymbol{X}, \tag{5.6}$$

and $\boldsymbol{X} \in \mathbb{R}^{r\times r}$ is a solution of a Riccati equation.

Finally, combining the estimator (5.3) and the full-information controller (5.5), we obtain the reduced-order controller (also called compensator or observer) of size r:

$$\dot{\hat{q}}(t) = (\boldsymbol{A}_r + \boldsymbol{B}_{2r}\boldsymbol{K} + \boldsymbol{L}\boldsymbol{C}_{2r})\hat{q}(t) - \boldsymbol{L}\boldsymbol{v}(t), \tag{5.7a}$$

$$\phi(t) = \boldsymbol{K}\hat{q}(t). \tag{5.7b}$$

At each instant in time, given only the measurements $\boldsymbol{v}(t)$, the compensator provides the control signal $\phi(t)$. The controller thus connects measurements from sensors to the actuators, which in combination with the Navier–Stokes system (3.1) results in a feedback closed-loop system, denoted by $\boldsymbol{G}_c$ hereafter.

When the external disturbances are white-noise processes, the 2-norm of the closed-loop system is a convenient measure of the input–output behaviour. The 2-norm of the closed-loop system $\boldsymbol{G}_c$ can be defined (Green & Limebeer 1995) as

$$\|\boldsymbol{G}_c\|_2^2 = \int_0^\infty |z|^2 \mathrm{d}t = \|z\|_{L^2(0,\infty)}^2. \tag{5.8}$$

So, the 2-norm of $\boldsymbol{G}_c$ equals the control objective (3.3) defined earlier (for the infinite time horizon) and can be calculated from the signals extracted by the output $\boldsymbol{C}_1$.

5.2. *Centralized versus decentralized approach*

The spatial localization of the actuators and the sensors requires a proper multivariable approach for the controller design. A simple approach is a *decentralized control*, where each actuator is connected only with one sensor (in our case, the corresponding upstream sensor); in such a controller, each loop can be regarded as a single-input-single-output (SISO) system and an equal number of actuators and sensors is required. If the decentralized controller is stable in each SISO loop and the inputs and the outputs are decoupled or only weakly coupled, then the closed loop is also stable.

For the TS wavepacket case, the decentralized approach yielded an unstable closed-loop system in numerical tests. A physical explanation is that the perturbation triggered in the boundary layer by the localized initial condition shown in figure 2 gradually spreads in the spanwise direction while propagating. This results in a dynamic coupling in the spanwise direction; thus, in this particular configuration, the decentralized approach is unfeasible since the spanwise coupling is disregarded. A second analysis is given by the relative gain array (RGA) matrix (Skogestad & Postlethwaite 2005, pp. 510–514), which provides a measurement of the degree of coupling among the inputs and the outputs of the system. Applying it to the reduced-order model, a strong coupling was found, confirming the presumption carried from the numerical tests.

Conversely, for the streaks case, the numerical tests resulted in a stable closed-loop system with both the approaches, although the closed-loop system built using the centralized design showed best performance. Moreover, the RGA matrix analysis suggested a weak degree of cross-coupling of the I/O system. From a physical point of view, this behaviour can be explained considering the strong elongation in the streamwise direction and the slow spanwise spreading of the streaks; these features result in a weak dynamical coupling in the spanwise direction. Nonetheless, a centralized approach accounts for the spanwise cross-coupling without disregarding it, resulting in more efficient disturbance mitigation.

In this work, we design a *centralized controller* for all cases (A–M and N–Q), i.e. all the actuators are connected with all the sensors used for estimation. Using the LQG approach, a centralized controller is guaranteed to result in a stable closed-loop system.

6. Control of TS wavepackets

In this section, the performance of the closed-loop system for the different sensor–actuator configurations listed in table 1 is investigated. In the reference case A, a *full* set-up is considered, where the row of actuators and the row of estimators consist of nine localized Gaussian elements equally spaced in the spanwise direction. Using this set-up, three cases are studied with different control penalty l (cases A–C) and four cases are analysed with different degree of noise contamination α (cases D–G); with $\alpha = 0.01$, case A can be considered to be an inexpensive controller when $l = 100$ (the controller effort is relatively cheap); case B is an intermediate case, with $l = 250$, whereas case C is an expensive case, with $l = 500$. In configurations D–G, the control penalty l is fixed, while the noise contamination parameter α is changed. Finally, for

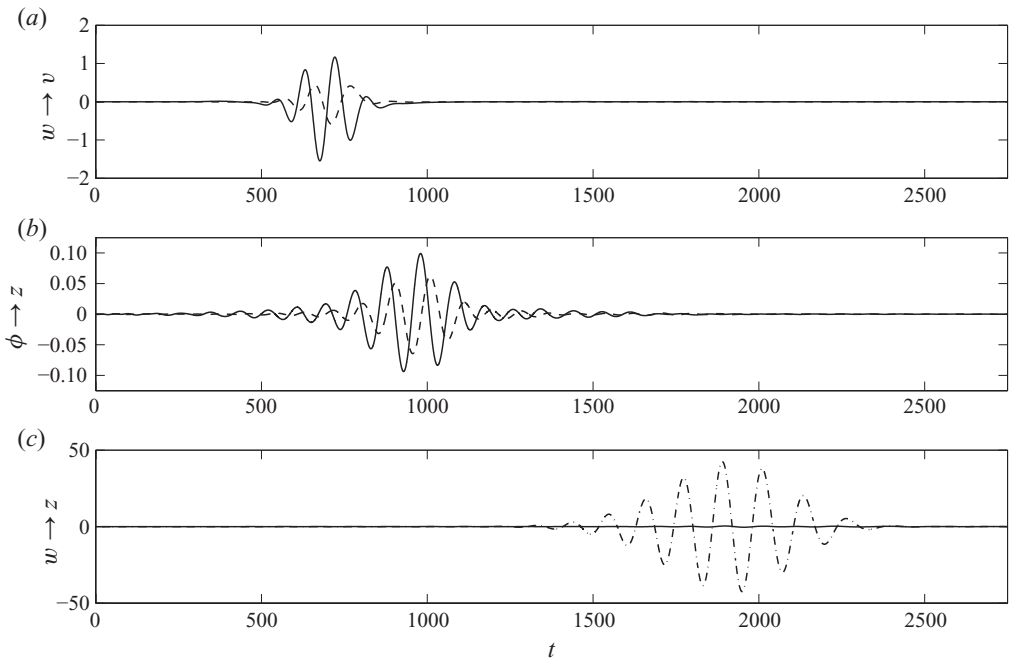

FIGURE 12. Input and output signals of the closed-loop system excited by an impulsive forcing. (*a*) Output signals extracted from $\boldsymbol{C}_{2,0}$, located in $(x, z) = (300, 0)$ (solid line), and $\boldsymbol{C}_{2,2}$, placed in $(x, z) = (300, +40)$ (dashed line). (*b*) The controller signals fed in $\boldsymbol{B}_{2,0}$ and $\boldsymbol{B}_{2,2}$ are indicated by a solid line and a dashed line, respectively. (*c*) Measurements extracted by the first sensor $\boldsymbol{C}_{1,1}$ for case A (solid) and the uncontrolled case (dash-dotted line).

the cases H–M, a reduced number of actuators and/or sensors is used, in order to investigate the dependence of the closed-loop performance on m and p.

We investigate the performance of the controlled closed-loop system and the uncontrolled Navier–Stokes system, when an impulsive forcing $w(t) = \delta(0)$ or a stochastic white-noise forcing is applied. We consider: (i) the impulse response (time signals), which provides a physical and direct measure of the control performance; (ii) the system 2-norm, which represents a total measure of the input–output behaviour and (iii) perturbation energy in the full spatial domain Ω.

In table 1, the 2-norm and the ratio between the peak energy and the initial disturbance energy is tabulated for each case. We observe a significant reduction of both measures. In the following section, these results are investigated further.

6.1. *Input–output analysis of the closed-loop system*

In figure 12, a few sensor measurements and actuator signals $\phi(t)$ for an impulse in $\boldsymbol{w}(t)$ pertaining to case A are shown. The location of actuators and sensors is shown schematically in figure 1. Figure 12(*a*) shows measurement signals used for estimation of the disturbance associated with the sensors $\boldsymbol{C}_{2,0}$ and $\boldsymbol{C}_{2,2}$ for an impulse in $\boldsymbol{B}_1$. The measurement detected by $\boldsymbol{C}_{2,0}$ (solid line) reveals a wavepacket structure of the evolving disturbance. The travelling disturbance reaches the sensor location at $t \approx 500$, in agreement with the estimated velocity of the wavepacket in a boundary layer ($\approx 0.47 U_\infty$). The element $\boldsymbol{C}_{2,2}$ (dashed line) shows an analogous behaviour, although a delay due to the spanwise spreading of the wavepacket is observed; moreover, the signal is characterized by a smaller amplitude.

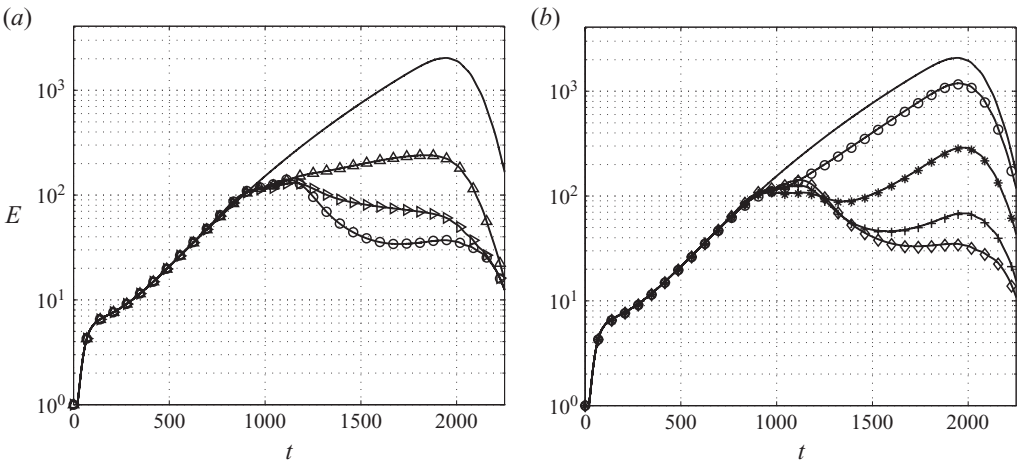

FIGURE 13. Kinetic energy as a function of time. In (*a*) and (*b*), the solid line shows the energy of $\boldsymbol{B}_1$. In (*a*), three closed-loop configurations for three different control penalties l are compared: —○—, a cheap case; —▷—, an intermediate case; —△—, an expensive case. In (*b*), the influence of noise corruption α on the performance is considered; the curves correspond to cases D–G: —◇—, D; — + —, E; — ⋆ —, F; —○—, G.

Figure 12(*b*) shows the control signals feeding the actuators $\boldsymbol{B}_{2,0}$ and $\boldsymbol{B}_{2,2}$; they are depicted by a solid line and a dashed line, respectively. In both cases, a time lag of 200 time units from the estimation signals is observed, to account for the advection of the waves from the location of the sensors to the location of the actuators array. The shift observed between the two signals is related to the 3D structure of the incoming perturbation. As mentioned previously, the actuator signals are computed using all the measurements extracted from $\boldsymbol{C}_2$. The control signal corresponds in fact to a cancellation signal; if the sensors were located at the same location as the actuators, a signal 180° out of phase with the control signal would be measured. Cancellation techniques, where a second wave of appropriate amplitude and phase cancel the travelling wave by interference, have been investigated for a long time (see e.g. Milling 1981). However, the main feature of the feedback approach adopted here is that no *a priori* knowledge of the functional behaviour of the controller is required and the controller is able to react to unexpected system uncertainties.

In figure 12(*c*), the output signal extracted from $\boldsymbol{C}_{1,1}$ (the first POD mode) is compared between the controlled case (solid line) and the uncontrolled case (dash-dotted line). It is clear that the amplitude of the closed-loop output signal is significantly reduced. Computing the system 2-norm, the performance can be evaluated by taking into account all the $k = 10$ signals extracted by $\boldsymbol{C}_1$. As shown in table 1, for case A, $\|\boldsymbol{G}_c\|_2^2 = 1.42$; this is a reduction of about 99 % of the 2-norm of the uncontrolled case ($\|\boldsymbol{G}\|_2^2 = 324.25$). As the controller effort is reduced, we observe higher values of $\|\boldsymbol{G}_c\|_2^2$ (case B, $\|\boldsymbol{G}_c\|_2^2 = 12.23$ and case C, $\|\boldsymbol{G}_c\|_2^2 = 55.27$). Increasing the degree of noise corruption of the signal leads to a worsening of the performance; in particular, this is evident when rather high values of α are considered; for instance, in case D, a reduction of about 99 % is observed ($\|\boldsymbol{G}\|_2^2 = 1.48$), whereas for cases F and G, $\|\boldsymbol{G}_c\|_2^2 = 209.03$ and $\|\boldsymbol{G}_c\|_2^2 = 318.74$, respectively.

6.2. *Perturbation energy and disturbance evolution*

Figure 13(*a*) shows the kinetic energy (in the full domain Ω) as a function of time for the uncontrolled case (solid line) and the controlled case A (—○—). The energy

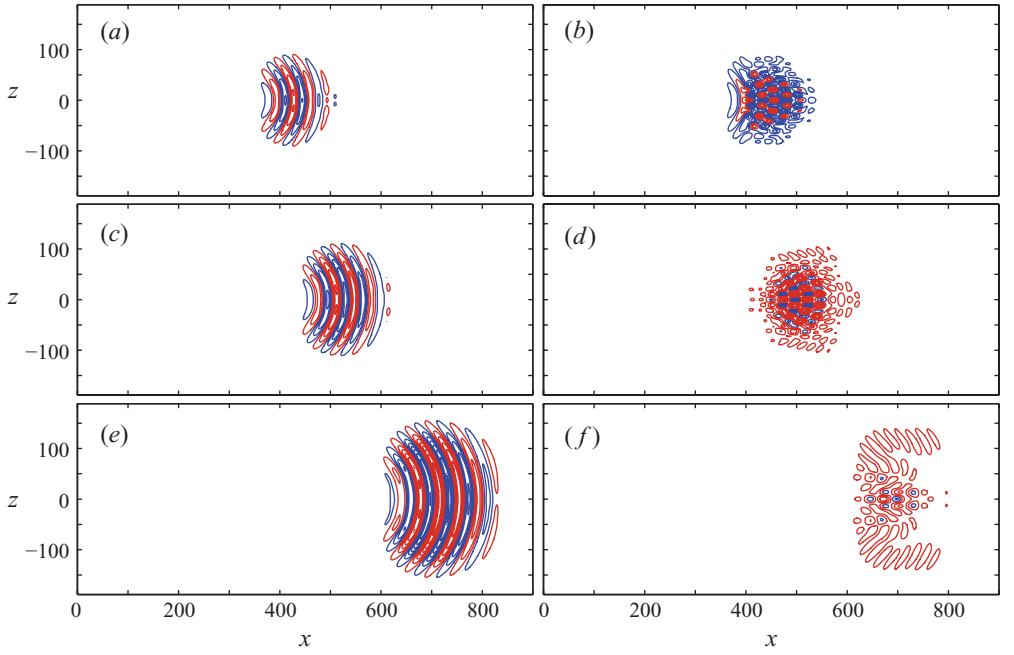

FIGURE 14. Evolution of a TS wavepacket at $t = 1000, 1250, 1750$, without control (a, c, e) and with control (b, d, f). The isocontours of the streamwise components are shown in the xz-plane at $y \approx 1.9$; red isolines indicate positive velocity, while the negative one is indicated by blue. All the plots are characterized by the same isocontour range $[-1.03, 1.03]$.

peak for the uncontrolled case is reached at $t \approx 1820$, with an energy amplification $E(t_{max})/E(0) = 2 \times 10^3$, whereas the controlled case shows one order of magnitude smaller peak value at $t \approx 1100$. Note that the controller is designed to reduce the norm of $\boldsymbol{C}_1$ and not the total kinetic energy of the flow. Nonetheless, by demanding the disturbance energy to be small at $\boldsymbol{C}_1$, the disturbance amplitude has to decrease significantly before it reaches the objective function. Therefore, minimization of disturbance energy in the region defined by $\boldsymbol{C}_1$ results in an actual reduction of the energy in the entire domain. The streamwise velocity component of the disturbance field at $t = 1000$, 1250 and 1750 for case A (left column) and the uncontrolled case (right column) are shown in figure 14. The isocontours display the flow field in the xz-plane at $y = 2$. At $t = 1000$, the perturbation is convected past the location $x = 400$, where the array of actuators is placed; the original structure is distorted into a more complicated 3D pattern, where traces of localized actuators are recognizable. At $t = 1250$, the perturbation appears to be mostly concentrated in the centre ($z \approx [-50, 50]$) of the domain, whereas the spanwise extension of the structures is significantly reduced. The original nearly 2D structure breaks down into a fully 3D structure. Finally, at $t = 1750$, a significant damping of the amplitude results in contour levels that are barely visible for case A, while the perturbation for the uncontrolled case attains its maximum energy. It is interesting to note that similar results were obtained by Sturzebecher & Nitsche (2003). They performed an experiment based on an adaptative controller designed to attenuate the TS instabilities; also in this case, the disruption of the original 2D structure resulted in a reduction of the disturbance level.

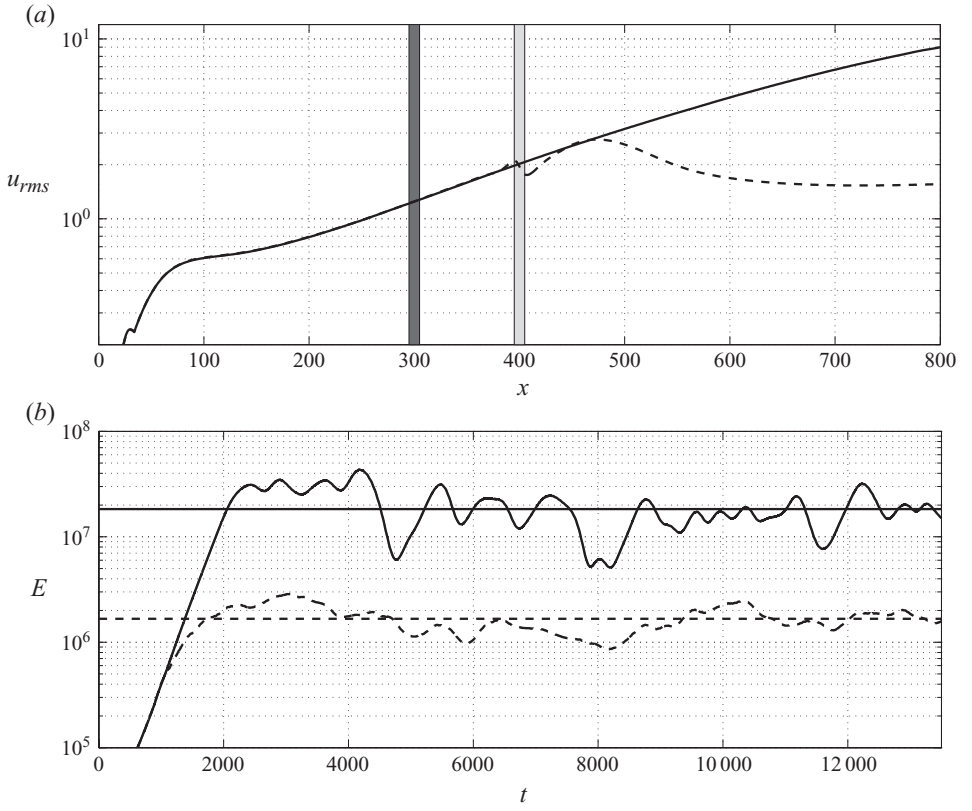

FIGURE 15. (*a*) The r.m.s. values of the uncontrolled system (solid line) and the controlled system A (dashed line). The location of the actuators and sensors is indicated by a lighter and darker region, respectively. (*b*) Perturbation energy versus time for a case forced by the stochastic white-noise signal $w(t)$ for an uncontrolled case (solid lines) and a controlled case (dashed lines); the horizontal lines represent the mean of the energy in the interval $t \in [2500, 12\,500]$.

Figure 13 also shows the performance of the *full* set-up controller for different choices of the penalty l (cases A–C). Note that for an intermediate value ($l = 250$, case B), the perturbation is characterized by a peak energy value close to the corresponding configuration with a cheap controller effort, although the norm $\|\boldsymbol{G}_c\|_2^2$ is higher. Case C (expensive controller) is the only configuration where the perturbation energy does not decay monotonically downstream of the actuators. When the noise corruption degree is considered as a parameter (cases D–G), an improvement is noticed, as expected, when smaller values of α are considered.

Figure 15(*a*) shows the behaviour of the controlled case A (dashed line) compared with the reference case, when the perturbation is excited with a stochastic white-noise forcing; the location of the actuators is indicated by a blue region, whereas the grey region indicates the location of the sensors. In the streamwise interval [390, 460], in the vicinity of the actuators, the r.m.s. value of the streamwise velocity component, after a small overshoot, begins to decay and at the end of the domain, it is nearly one order of magnitude smaller than the uncontrolled flow. The behaviour of the disturbance energy in time is shown in figure 15(*b*); the mean values indicate a reduction of

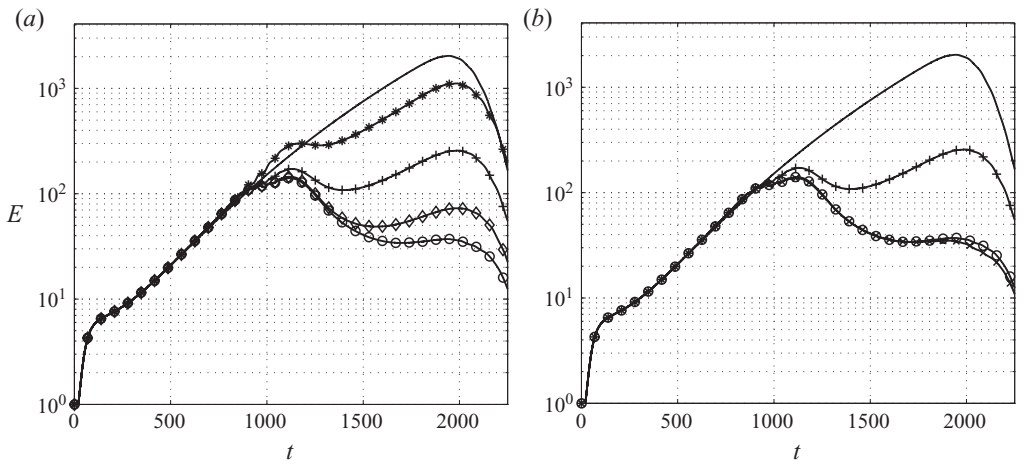

FIGURE 16. Kinetic energy as a function of time. In (*a*) and (*b*), the solid line shows the energy of $\boldsymbol{B}_1$. In (*a*), cases H ($-\star-$), I ($-+-$), L ($-\diamond-$) and A ($-\circ-$) are characterized by 3, 5, 7 and 9 actuators, respectively. In (*b*), the curves correspond to cases I ($-+-$), M ($-\times-$) and A ($-\circ-$) with 5, 5 and 9 sensors, respectively.

one order of magnitude of the energy amplitude and a significant reduction in the fluctuation (i.e. variance) is observed for the controlled case.

6.3. *Influence of the number of sensors and actuators*

The norm $\|\boldsymbol{G}_c\|_2^2$ and the energy amplification for cases D–F are reported in table 1. It can be concluded that controllers with a lower number of actuators than case A ($m=9$) are still able to reduce the norm $\|\boldsymbol{G}_c\|_2^2$ significantly, whereas there is a somewhat less efficient reduction in the perturbation energy amplification.

Figure 16(*a*) shows the energy behaviour for cases H–L in addition to the reference case A and the uncontrolled case. A gradual improvement of the performance is observed when the number of actuators is increased. Indeed, by increasing the number of the equidistant actuators, it is possible to cover a wider region in the spanwise direction. As a consequence, a considerable reduction in the energy growth is observed only when a sufficiently wide region in the spanwise direction is spanned by the actuator array. In particular, case H ($m=3$, $p=3$) can be considered an example of insufficient actuation; in figure 16(*a*), we notice an initial overshoot of the energy in the interval $t\in[1000, 1200]$, when the controller begins to act, and a weak energy reduction. Moreover, the spatial evolution of the perturbation, not shown here, is similar to the uncontrolled case, indicating a weak influence of the actuator on the perturbation structure.

Figure 16(*b*) shows the influence of the number of sensors (cases I and M). The energy curve for case A ($m=9$), obtained with nine estimators, is hardly distinguishable from the curve obtained with the controller designed for case M, based only on five estimators. The array of sensors is located further upstream than the array of actuators, where the spanwise extension of the TS wavepacket is smaller. Therefore, the sensors located on the flanks have a nearly insignificant contribution to the estimation of the disturbance.

7. Control of streaks

The performance of the closed-loop system in the case of streaks is investigated considering three different configurations, see table 2. In all cases, the rows of actuators

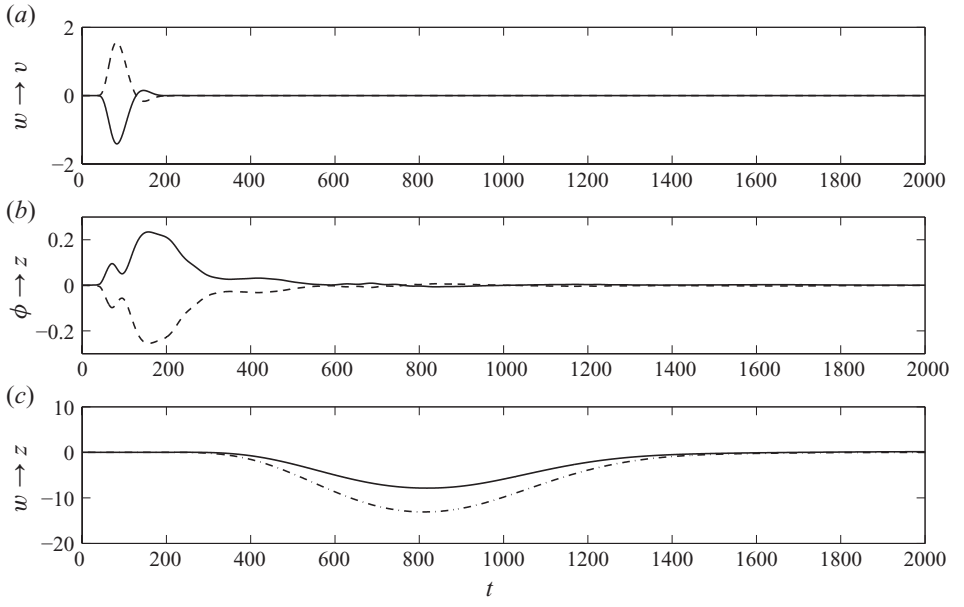

FIGURE 17. Input and output signals of the closed-loop system N excited by an impulsive forcing. (*a*) Output signals extracted from $\boldsymbol{C}_{2,1}$, located in $(x, z) = (100, 4)$ (dashed line), and $\boldsymbol{C}_{2,-1}$, placed in $(x, z) = (100, -4)$ (solid line). (*b*) The controller signals fed in $\boldsymbol{B}_{2,1}$ and $\boldsymbol{B}_{2,-1}$ are indicated by a solid line and a dashed line, respectively. (*c*) Measurements extracted by the first sensor $\boldsymbol{C}_{1,1}$ for case N (solid) and the uncontrolled case (dash-dotted line).

and sensors consist of eight localized Gaussian elements, equally spaced in the spanwise direction ($\Delta_z = 4$). More details are sketched in figure 1, where the location of the elements is depicted. The parametric investigation is carried out considering three different control penalties l: the reference case N is a cheap controller with $l = 50$; case O is an intermediate case with $l = 100$, whereas case P is the expensive case, with $l = 150$. The description of the results closely follows the steps considered previously for the TS control, using (i) the impulse response (time signals), (ii) the 2-norm of the system and (iii) the perturbation energy in the full domain.

7.1. *Input–output analysis and disturbance evolution*

Figure 17(*a–c*) shows measurements extracted from the system and actuator signals $\phi(t)$ for the reference case N. In particular, figure 17(*a*) reports the signals extracted for the estimation from the sensors $\boldsymbol{C}_{2,+1}$ and $\boldsymbol{C}_{2,-1}$, depicted by a dashed line and a solid line, respectively. The signals are opposite in phase, since the perturbation is antisymmetric with respect to the xy-plane ($z = 0$). The sensors register the disturbance at $t \approx 100$, in accordance with the estimated velocity of propagation of a streak in a boundary layer (≈ 0.80–$0.85U_\infty$). The signal amplitude reaches its maximum at $t \approx 150$, after which it decays. The actuators $\boldsymbol{B}_{2,+1}$ and $\boldsymbol{B}_{2,-1}$ are fed with the signals shown in figure 17(*b*) by a solid and dashed line, respectively. The actuation is activated as soon as the sensors detect the incoming perturbation. It is interesting to note that the actuator signal has a sign opposite to the corresponding sensor measurement: a positive measurement extracted by the sensor coincides with a negative actuation signal further downstream and vice versa, similar to the so-called opposition control (Hammond *et al.* 1998).

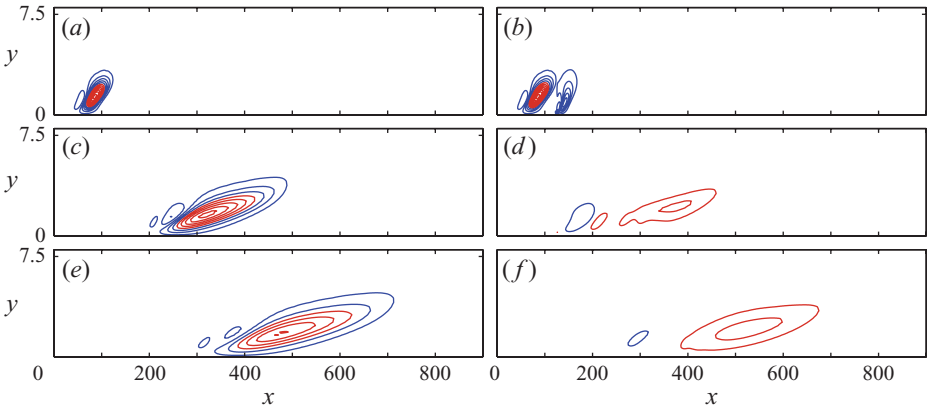

FIGURE 18. Impulse response to a localized initial condition triggering the lift-up effect at $t = 100, 500, 750$. The isocontours of the streamwise component are shown in the xy-plane at $z = 4$ without control (a, c, e) and with control (b, d, f). Positive velocity is indicated by red contours, while blue contours indicate negative velocity; all the plots have the same isocontour range $[-0.65, 0.65]$.

Finally, figure 17(c) shows the measurements extracted from the sensor $\boldsymbol{C}_{1,+1}$ for both the controlled case (solid line) and the reference uncontrolled case (dash-dotted line). A reduction in the signal amplitude is observed, although the overall performance is worse than for the TS case. Figure 18 shows the streamwise velocity component for the uncontrolled case (left column) and the controlled case H (right column); the isocontours display the flow field in the xy-plane at $z = 1.5$ for three instants of time, $t = 100, 500, 750$. The same isocontour levels are considered for each instant of time. As previously noticed, the controller action starts as soon as the perturbation reaches the estimation sensors located at $x = 75$; indeed, it is possible to notice at $t = 100$ the action of the controller in $x = 125$. At $t = 500$, the perturbation has travelled further downstream, while being reduced by the controller. The structure of the perturbation, shown in figure 18(d), is similar to the uncontrolled case in figure 18(c), although of lower amplitude. Final decay due to the viscous effects is observed at $t = 750$ in both the cases. The streak is disrupted by the actuation at the wall. The effect of the control on the evolving perturbation is similar to the reactive controller implemented by Lundell (2007) and the modulated blowing/suction used by the same author in a previous work (Lundell 2003).

In table 2, the performance of the controllers with various control penalties is quantified by the 2-norm of the transfer function $\boldsymbol{G}_c$. A reduction of about 66 %, 30 % and 16 % of the 2-norm of the transfer function $\boldsymbol{G}_c$ is reported for the cheap (case N), intermediate (case O) and the expensive controller (case P), respectively.

7.2. *Perturbation energy*

Figure 19 shows the kinetic energy of the streak disturbance in the full domain Ω as a function of time. The uncontrolled case is indicated by a solid line and it is characterized by an energy amplification $E(t_{max})/E(0) = 3 \times 10^2$, occurring at $t \approx 350$. The cheap controller ($l = 50$) and the intermediate controller ($l = 100$) give an initial peak at $t \approx 180$, followed by the decay of the perturbation amplitude; in both cases, a reduction of about 33 % of the energy peak is observed. Although the energy peaks are almost comparable for the controllers N and O, the first one is more aggressive and shows a stronger damping of the energy amplitude for $t \approx 200$.

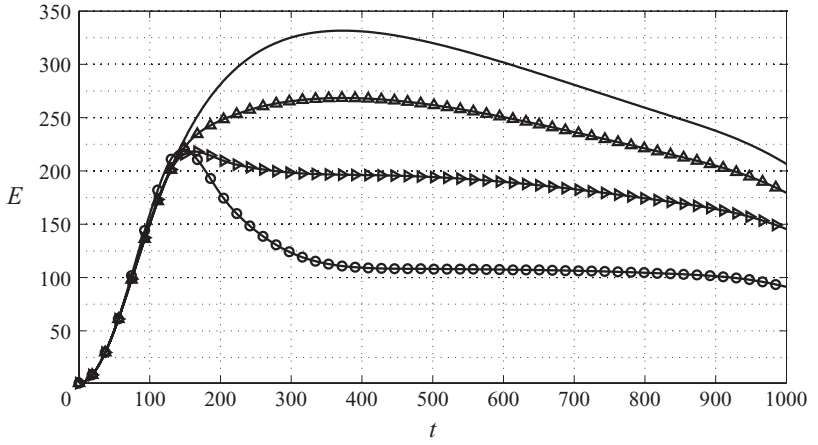

FIGURE 19. Disturbance energy as a function of time for the streaks. The uncontrolled reference case St0 is represented by a solid line. The closed-loop configurations listed in table 2 are shown: —○—, the cheap case N; —▷—, the intermediate case O; —△—, the expensive case P.

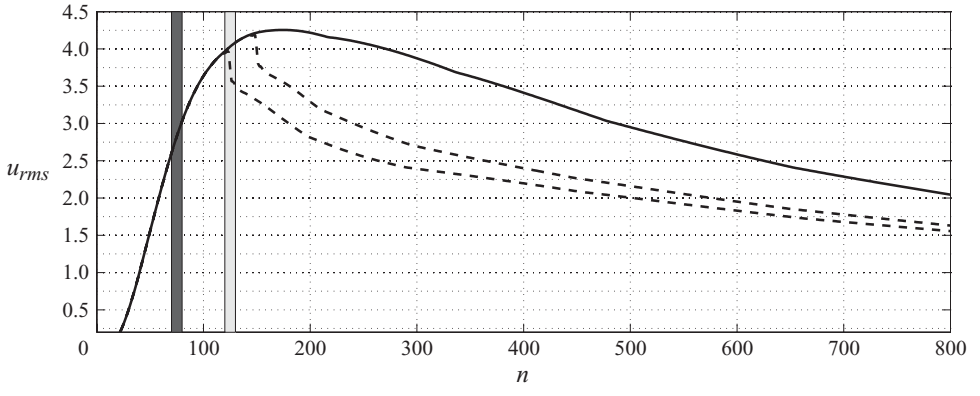

FIGURE 20. The r.m.s. values of the uncontrolled system (solid line), the controlled system N (dashed line) and the controller system Q (dashed, thinner line). For case N, the location of the actuators and sensors is indicated by a lighter and darker grey region, respectively.

Figure 20 shows the behaviour of the controlled cases N and Q compared with the reference case, when the perturbation is excited with a stochastic force (white noise); the r.m.s. of the streamwise velocity is considered along the streamwise direction. The aim of this analysis is twofold: understanding how the controller behaves along the x-coordinate and providing some insights into the influence of a different location of the arrays. In all the cases, a quick drop of the r.m.s. values is observed at the location of the actuators, where the controller starts to act on the perturbation. The configuration in case N allows a larger reduction of the maximum u_{rms} (figure 19). The performance degrades when the actuators are located further upstream. The perturbation energy increases at the actuators location, and the r.m.s. values slowly decay downstream ($x \geqslant 150$); thus, although the actuator is still able to quench the perturbation, the increased energy reduces the overall performance of the controller. This can be explained by a larger estimation error: the estimator can correctly capture the streaks (streamwise velocity perturbation) downstream rather than vortices upstream

(cross-stream velocity components); this error is related to the efficiency of the low-order model.

The control performance subject to stochastic excitations indicates that the controller is able to continuously react to different temporal scales, which is encountered for example in the presence of free-stream turbulence (FST).

8. Discussion and remarks

In this section, we discuss the results presented above in the context of practical implementation and future development of our investigation. The fully 3D set-up makes the present controller close to possible experimental implementation, where localized actuators and sensors are used. It is possible to use numerical studies to gain valuable information about the experimental set-up beforehand and to compute the control gains that will be implemented. The sensors and the actuators ($\boldsymbol{C}_2$ and $\boldsymbol{B}_2$, respectively) can be modelled as localized volume forcing. The objective function $\boldsymbol{C}_1$ can be defined either numerically or using an array of sensors. In particular, the first choice relies on the possibility of reproducing a POD approach as that we followed in the control design once the upstream disturbance $\boldsymbol{B}_1$ is modelled. Here, optimal initial conditions were used to show the feasibility of the control, but, in general, the choice of the upstream disturbance $\boldsymbol{B}_1$ is closely related to the environment that one desires to reproduce. For instance, the perturbation arising from FST can be modelled using a projection over a finite number of optimal modes (Tempelmann, Hanifi & Henningson 2010). Conversely, in a low-noise environment, where TS waves dominate, localized initial conditions distributed in the spanwise direction can spontaneously generate packets of TS waves. Once the inputs and outputs are modelled, the LQG compensator can be easily designed following the procedure explained; moreover, numerical tests can help in determining the most efficient form of actuation, provided these are correctly modelled in the simulations. The location and number of sensors and actuators is also easier to test in a simulation than in a laboratory. Useful information can be obtained in this case by examining the spatial structure of the direct and adjoint balanced modes. In this respect, our results suggest that, for an effective implementation of the feedback control of a 3D wavepacket in a boundary layer, actuation may be more crucial than sensing and estimation of incoming disturbances. This is in agreement with the recent empirical observations in Monokrousos, Lundell & Brandt (2010*b*).

A further strategy directly applicable in experiments relies on a system identification algorithm, known as the eigensystem realization algorithm (ERA). This represents an approach formally equivalent to the model reduction procedure discussed here; for more details, we refer to Ma, Ahuja & Rowley (2009). This technique allows the identification of a model for the system from the input/output analysis and is thus particularly well-suited to the experimental set-up. Once the model is identified from the experimental data, it is possible to design an appropriate LQG controller for the experiment. However, information about balanced modes, sensitivity and spatial structures of the most amplified perturbations is not accessible in this way.

The choice of actuators/sensors and their placement was decided mainly by following physical arguments based on the knowledge of the instabilities. To control TS wavepackets, the array of actuators was placed in the centre of the box. Indeed, after the actuation, the perturbation recovers the spanwise coherence and experiences new energy growth, similar to that achieved during the first stage (see figure 14*f*). However, this behaviour clearly suggests the need of introducing a

repeated streamwise actuation, as shown in Sturzebecher & Nitsche (2003). The introduction of multi-stage actuation can improve the overall performance of the device, moving the transition location further downstream. Moreover, using successive arrays it is possible to target instabilities of different frequency growing at different Reynolds numbers (different streamwise regions), or perturbations that arise in the presence of adverse pressure gradients.

To control streaks, two different set-ups located in different streamwise positions were tested; an improvement of the overall performance (around $\approx 15\,\%$) was observed when the sensors and actuators were further upstream. Note that in the case streaks are induced by FST, there is a longer upstream region of streak growth; moreover, the streaks we introduced are optimal and characterized by a fast energy growth. Therefore, in the presence of external FST, the estimation/control can be more effective. As shown before, and in agreement with the experimental results of Lundell (2007), streaks are damped at the location of actuators. However, streaks can be regenerated early with the presence of FST, see Monokrousos *et al.* (2008). Thus, repeated control can also be exploited here by introducing a number of arrays acting at different positions in the streamwise direction.

The possibility of placing more than one actuation array and their interaction was also investigated. We performed numerical tests – not reported here – where the TS controller and the streak controller were simultaneously active, in the presence of a TS wave, streaks or a linear combination of the two optimal initial conditions. We observed that the streaks controller damped only the streaky structures, while the set-up further downstream quenched only the TS waves. The behaviour can be interpreted considering the POD-based objective function, which is completely different in the two cases, so that one type of disturbance is transparent to the controller designed for the other type. In other words, the TS controller did not react in the presence of streaks, whereas it was effective when TS packets were introduced, and vice versa the streak controller did not react in the presence of TS packets. Note that this framework allows building of a reduced-order model able to act on disturbances that have different time- and length scales.

Finally, for a practical implementation, we have to account for unavoidable modelling errors; in the present paper, we assumed a perfect knowledge of the flow parameters, but, in general, a practical implementation of the control needs to guarantee robust performance when uncertainties are present as well. The optimal control framework used here does not account explicitly for uncertainties; however, it is important to note that the behaviour of the controller can nonetheless be robust enough to small deviation of the flow parameters. Using numerical simulations, it is possible to verify the robustness of the controller. In figure 21(*a, b*), two examples are shown: deviation from the design, Reynolds number, and behaviour in the presence of an adverse pressure gradient. In the first case, for a deviation of $\pm 5\,\%$ of the nominal Reynolds number, it is still possible to achieve good performance. Further investigation at higher Reynolds numbers revealed a progressive worsening of the performance, analogous to that we observed with fewer actuators. The presence of an adverse pressure gradient introduces a strong change in the propagation of the wavepackets, both in terms of amplification and propagation speed; a Falkner–Skan–Cooke (FSC) boundary layer is considered, with $m = -0.025$, see Schlichting & Gersten (2000). As expected from linear stability theory, the disturbance energy shows a larger amplification, $E_{max}/E_0 \approx 1.3 \times 10^6$ (figure 20*b*). In this case, the controller used for case A is still able to reduce the magnitude of the energy peak by almost one order of magnitude, but the result is overall less satisfactory than for the nominal pressure

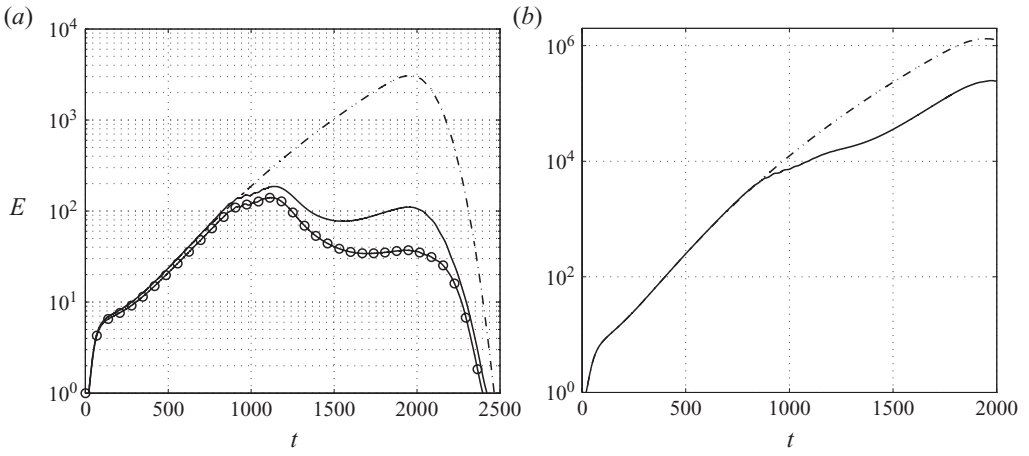

FIGURE 21. Perturbation energy as a function of time for TS wavepackets at two off-design conditions. The controlled cases are obtained using the controller A. (*a*) Kinetic energy versus time for the TS wave propagating at $Re = 1050$ is represented by a dash-dotted line. A solid line indicates the behaviour of the controller in off-design conditions, whereas the dotted line is related to the same controller acting at design conditions. (*b*) Perturbation energy evolution for a wavepacket evolving in the presence of an adverse gradient pressure ($m = -0.025$). The solid line denotes the controlled case.

gradient. The difference in the performance is mainly attributed to the different speed of the travelling unstable waves, which makes the actuation slightly out of phase. In addition, since the estimator is expecting lower amplifications, the control signal is weaker than necessary. To conclude, it is worthwhile to point out that a more robust controller can be included in this framework. An example is given by the $\mathscr{H}_\infty$ approach (Dullerud & Paganini 1999).

9. Conclusion

Using systematic methods from control theory in combination with localized sensing/actuation, it is possible to reduce the growth of small-amplitude 3D disturbances in the boundary layer. To this end, we have built low-dimensional models ($r = 60$) that capture the input–output behaviour of the flat-plate boundary layer, and used these models for the optimal feedback control design. The initial conditions considered provide the maximum energy growth for a given final time; in particular, we demonstrated that the energy of 3D TS wavepacket, obtained for long-time optimization, is damped by two orders of magnitude using nine sensors for estimation and nine actuators. The control performance was also investigated with a reduced number of sensors and actuators in the configuration; it was found that a smaller number of actuators decreases significantly the effectiveness of the controller, whereas a reduced number of sensors has a smaller impact on the performance. When a short time of optimization is considered, an initial condition triggering a streaky wavepacket is obtained; in this case, the perturbation energy can be damped using eight sensors each for the estimation and actuation.

Although the significant reduction of perturbation energy for transition control remains to be tested, such a drastic energy reduction is likely to result in a delay of the initial stages of the transition process. If the actuators and sensors represent realistic models of physically feasible devices, it is possible to use the low-dimensional

controller designed numerically in laboratory experiments. The fact that we have modelled the inputs and outputs as volume forcing does not mean that they cannot be implemented experimentally. It is the effect of an actuator that is important to model, and not the actuator itself. Another issue that needs to be taken into account for a real application is control robustness. If the numerically designed controller is used in laboratory experiments, it is unavoidable that some parameters, such as the Reynolds number and pressure gradients, will vary. We showed that the controllers are robust to a strong deviation of the Reynolds number, whereas the performance was less satisfactory at an off-design pressure gradient. Fortunately, modern developments in robust control theory may be used to rigorously incorporate uncertainties that may be present in the design process. The method for optimal control presented in this paper can be incorporated into such a robust control framework.

The authors thank A. Monokrousos, for providing the optimal initial conditions and for fruitful discussions, and M. Ilak, for the detailed comments on the manuscript. Computer time provided by SNIC (Swedish National Infrastructure for Computing) is gratefully acknowledged. This work was partially sponsored by the Air Force Office of Scientific Research, through the European Office EOARD, under grant/contract number FA8655-10-M-4006. The authors also acknowledge financial support from the Swedish Research Council (VR).

Appendix A. Adjoint Navier–Stokes equations

In this section, the adjoint Navier–Stokes equations are given for the sake of completeness. A detailed derivation is provided by Bagheri *et al.* (2009*b*).

The adjoint velocity field and the adjoint pressure field are denoted by $\boldsymbol{p}(\boldsymbol{x},t)=(u^*,v^*,w^*)$ and $\sigma(\boldsymbol{x},t)$, respectively. Considering the boundary conditions (2.3) used for $\boldsymbol{u}$ and requiring that $\boldsymbol{p}=(u^*,v^*,w^*)$, p and σ satisfy

$$\boldsymbol{p}\,(0,y,-L_z/2)=\boldsymbol{p}\,(x,y,L_z/2)\,, \tag{A 1a}$$

$$\boldsymbol{p}\,(0,y,z)=\boldsymbol{p}\,(L_x,y,z)\,, \tag{A 1b}$$

$$\boldsymbol{p}\,(x,0,z)=\boldsymbol{p}\,\big(x,L_y,z\big)=0, \tag{A 1c}$$

$$p\,(0,y,-L_z/2)=p\,(L_x,y,L_z/2)\,, \tag{A 2a}$$

$$\sigma\,(0,y,-L_z/2)=\sigma\,(L_x,y,L_z/2)\,, \tag{A 2b}$$

and the adjoint of the linearized Navier–Stokes equations (3.1) associated with the inner product $\langle\cdot,\cdot\rangle_\Omega$ is given by

$$-\frac{\partial\boldsymbol{p}}{\partial t}=(\boldsymbol{U}\cdot\nabla)\,\boldsymbol{p}-(\nabla\boldsymbol{U})^{\mathrm{T}}\,\boldsymbol{p}+\nabla\sigma+Re^{-1}\nabla^2\boldsymbol{p}+\lambda_f(x)\boldsymbol{p}, \tag{A 3a}$$

$$0=\nabla\cdot\boldsymbol{p}, \tag{A 3b}$$

$$\boldsymbol{p}=\boldsymbol{p}_T\quad\text{at } t=T. \tag{A 3c}$$

The code described by Chevalier *et al.* (2007*b*), based on a Chebyshev–Fourier series approximation, is used for both the forward and adjoint simulations. Using this approximation, the discrete operators $\hat{\boldsymbol{A}}$, $\hat{\boldsymbol{B}}$ and $\hat{\boldsymbol{C}}$ and the respective adjoint operators can be defined. As in the case of the forward system, the adjoint equations (A 3) can be cast as an initial-value problem,

$$-\dot{\boldsymbol{p}}(t)=\hat{\boldsymbol{A}}^*\boldsymbol{p}(t),\quad \boldsymbol{p}(T)=\boldsymbol{p}_T, \tag{A 4}$$

where the action of $\hat{\boldsymbol{A}}^*$ corresponds to evaluating the right-hand side of (A 3), including the boundary conditions. The evolution operator $\boldsymbol{T}^*$ associated with $\hat{\boldsymbol{A}}^*$ is defined as

$$\boldsymbol{p}(-t) = \boldsymbol{T}^*(t)\boldsymbol{p}(T). \tag{A 5}$$

Given an initial condition, the adjoint evolution operator $\boldsymbol{T}^*$ provides the resulting flow field at time $-t$.

Appendix B. Analytical expressions of actuators and sensors

Each element of the arrays $\boldsymbol{B}_2$ and $\boldsymbol{C}_2$ is a localized Gaussian function

$$\boldsymbol{h}(\boldsymbol{x}, \boldsymbol{x}_0) = \begin{pmatrix} \sigma_x \hat{y} \\ -\sigma_y \hat{x} \\ 0 \end{pmatrix} \exp\left(-\hat{x}^2 - \hat{y}^2 - \hat{z}^2\right), \tag{B1a}$$

where

$$\hat{x} = \frac{x - x_0}{\sigma_x}, \quad \hat{y} = \frac{y}{\sigma_y}, \quad \hat{z} = \frac{z - z_0}{\sigma_z}. \tag{B1b}$$

The scalar quantities appearing in the denominator define the size of the Gaussian spatial distribution close to the wall and are equal for all the elements; for the TS waves, we considered $(\sigma_x, \sigma_y, \sigma_z) = [5, 1.5, 6]$, whereas for the streaks we used $(\sigma_x, \sigma_y, \sigma_z) = [1.75, 2, 2]$. All the elements of the arrays have the same spatial shape; the position in the plane xz is given by $\boldsymbol{x}_0$ and is contained for all the test cases in tables 1 and 2. From this definition, we obtain

$$\boldsymbol{B}_2 = \left[\boldsymbol{h}\left(\boldsymbol{x}, \boldsymbol{x}_{\phi,1}\right), \boldsymbol{h}\left(\boldsymbol{x}, \boldsymbol{x}_{\phi,2}\right), \ldots, \boldsymbol{h}\left(\boldsymbol{x}, \boldsymbol{x}_{\phi,m}\right)\right] \tag{B2}$$

and

$$\boldsymbol{C}_2\boldsymbol{u} = \int_\Omega \begin{pmatrix} \boldsymbol{h}\left(\boldsymbol{x}, \boldsymbol{x}_{v,1}\right)\boldsymbol{u} \\ \ldots \\ \boldsymbol{h}\left(\boldsymbol{x}, \boldsymbol{x}_{v,p}\right)\boldsymbol{u} \end{pmatrix} \mathrm{d}x\,\mathrm{d}y\,\mathrm{d}z, \tag{B3}$$

where m and p indicate the number of actuators and sensors, respectively. Each element of $\boldsymbol{B}_2$ and $\boldsymbol{C}_2$ is denoted by a second subscript. The actuators mimic a manipulation on the flow close to the wall; the measurements are extracted by averaging the velocity field using the Gaussian function as weights.

Denoting by $\boldsymbol{p}(\boldsymbol{x}, t) = (u^*, v^*, w^*)$ the adjoint velocity field, the adjoints of the input and output operators $\boldsymbol{B}_2$ and $\boldsymbol{C}_2$, associated with the inner product $\langle \cdot, \cdot \rangle_\Omega$, are

$$\boldsymbol{B}_2^*\boldsymbol{p} = \int_\Omega \begin{pmatrix} \boldsymbol{h}\left(\boldsymbol{x}, \boldsymbol{x}_{\phi,1}\right)\boldsymbol{p} \\ \ldots \\ \boldsymbol{h}\left(\boldsymbol{x}, \boldsymbol{x}_{\phi,m}\right)\boldsymbol{p} \end{pmatrix} \mathrm{d}x\,\mathrm{d}y\,\mathrm{d}z \tag{B4}$$

and

$$\boldsymbol{C}_2^* = \left[\boldsymbol{h}\left(\boldsymbol{x}, \boldsymbol{x}_{v,1}\right), \boldsymbol{h}\left(\boldsymbol{x}, \boldsymbol{x}_{v,2}\right), \ldots, \boldsymbol{h}\left(\boldsymbol{x}, \boldsymbol{x}_{v,p}\right)\right]. \tag{B5}$$

Hereinafter, the notation adopted in the next sections will denote the continuous operator; the discretized operators will be indicated by a hat. Note that the hat is omitted in the article.

Appendix C. Balanced truncation for model reduction

In this section, the basic concepts for balanced truncation – controllability, observability and the *Hankel operator* – are briefly recapitulated in a simplified discrete form; for more details, we refer to Bagheri *et al.* (2009*b*), where the Hilbert spaces and the norms used are introduced for the definition of the continuous operators and the related adjoint operators.

The relation between the inputs and outputs of the system can be described by considering the formal solution of the input–output system (3.1). Introducing the input vector $\boldsymbol{f}(t) = (\boldsymbol{w}, \boldsymbol{g}, \phi)^{\mathrm{T}} \in \mathbb{R}^{(m+2)}$ and the output vector $\boldsymbol{y}(t) = (\boldsymbol{z}, \boldsymbol{v})^{\mathrm{T}} \in \mathbb{R}^{(p+k)}$, we can rewrite the system (3.1) in the standard state-space form as

$$\dot{\boldsymbol{u}}(t) = \hat{\boldsymbol{A}}\boldsymbol{u}(t) + \hat{\boldsymbol{B}}\boldsymbol{f}(t), \tag{C1a}$$

$$\boldsymbol{y}(t) = \hat{\boldsymbol{C}}\boldsymbol{u}(t) + \hat{\boldsymbol{D}}\boldsymbol{f}(t), \tag{C1b}$$

where $\hat{\boldsymbol{B}} = (\hat{\boldsymbol{B}}_1, 0, \hat{\boldsymbol{B}}_2)$, $\hat{\boldsymbol{C}} = (\hat{\boldsymbol{C}}_1, \hat{\boldsymbol{C}}_2)^{\mathrm{T}}$ and $\hat{\boldsymbol{D}} \in \mathbb{R}^{(p+k)\times(m+2)}$,

$$\hat{\boldsymbol{D}} = \begin{pmatrix} 0 & 0 & \boldsymbol{I}_l \\ 0 & I_\alpha & 0 \end{pmatrix}. \tag{C2}$$

The solution of the system (C1) is given by

$$\boldsymbol{y}(t) = \hat{\boldsymbol{G}}\boldsymbol{f}(t) = \hat{\boldsymbol{C}} \int_{-\infty}^{t} \boldsymbol{T}(t-s)\hat{\boldsymbol{B}}\boldsymbol{f}(s)\,\mathrm{d}s, \tag{C3}$$

assuming both the initial condition $\boldsymbol{u}_0$ and the term $\hat{\boldsymbol{D}}$ to be zero. The linear mapping $\hat{\boldsymbol{G}} : L^2(-\infty, \infty) \to L^2(-\infty, \infty)$ between the inputs $\boldsymbol{f}(t)$ and outputs $\boldsymbol{y}(t)$ is a causal input–output operator. Both the signals and the system $\hat{\boldsymbol{G}}$ can be represented in the frequency domain. A Laplace transform of (C3) results in a transfer function matrix

$$\boldsymbol{y}(s) = \tilde{\boldsymbol{G}}(s)\boldsymbol{f}(s) = (\hat{\boldsymbol{C}}(s\boldsymbol{I} - \hat{\boldsymbol{A}})^{-1}\hat{\boldsymbol{B}})\boldsymbol{f}(s), \tag{C4}$$

with $s \in \mathbb{C}$. Henceforth, the tilde on $\tilde{\boldsymbol{G}}$ is omitted since it is related to $\boldsymbol{G}$ by a linear transformation.

The mapping $\hat{\boldsymbol{G}}$ is not a finite-rank operator: thus, a second finite-rank mapping is introduced. For the given system $\hat{\boldsymbol{G}}$, the Hankel operator $\hat{\boldsymbol{H}} : L^2(-\infty, 0] \to L^2[0, +\infty)$ is defined as

$$\boldsymbol{y}(t) = \hat{\boldsymbol{H}}\boldsymbol{f}(t) = \hat{\boldsymbol{C}} \int_{-\infty}^{0} \boldsymbol{T}(t-s)\hat{\boldsymbol{B}}\boldsymbol{f}(s)\,\mathrm{d}s. \tag{C5}$$

The Hankel operator is closely related to the *controllability* and *observability* operators. In particular, the controllability operator $\hat{\boldsymbol{L}}_c : L^2(-\infty, 0] \to \mathbb{U}$ is defined as

$$\boldsymbol{u}_0 = \hat{\boldsymbol{L}}_c\boldsymbol{f}(t) = \int_{-\infty}^{0} \boldsymbol{T}(-s)\hat{\boldsymbol{B}}\boldsymbol{f}(s)\,\mathrm{d}s, \tag{C6}$$

and maps past input signals $\boldsymbol{f}(t)$ to an initial state $\boldsymbol{u}_0$. The action of $\hat{\boldsymbol{L}}_c$ is numerically approximated by the time-stepper that computes the response of the system governed by the linearized Navier–Stokes equations forced by $\boldsymbol{f}(t)$ with a zero initial condition. The second operator, the observability operator $\hat{\boldsymbol{L}}_o$, provides a dual action and maps the state $\boldsymbol{u}_0$ to future outputs, $\hat{\boldsymbol{L}}_o : \mathbb{U} \to L^2[0, +\infty)$; it is defined as

$$\boldsymbol{y}(t) = \hat{\boldsymbol{L}}_o\boldsymbol{u}_0 = \hat{\boldsymbol{C}}\boldsymbol{T}(t)\boldsymbol{u}_0, \quad t \geqslant 0. \tag{C7}$$

Using the above definitions, the Hankel operator can be seen as the combination of the two operators:

$$\hat{\boldsymbol{H}} = \hat{\boldsymbol{L}}_o \hat{\boldsymbol{L}}_c. \tag{C8}$$

Note that the operator $\hat{\boldsymbol{H}}$ has at most rank n for a state space of order n. Indeed, an input is driven via $\hat{\boldsymbol{L}}_c$ to an initial state $\boldsymbol{u}_0$ and each output can be determined from the knowledge of the state $\boldsymbol{u}_0$. Since each state $\boldsymbol{u}_0$ is determined uniquely from an input, two linearly independent states will produce two linearly independent future outputs; thus, the rank of the operator $\hat{\boldsymbol{H}}$ cannot exceed the dimension of the state space n.

C.1. *Adjoint operators*

Using the adjoint of the inputs and outputs introduced in (B4) and (B5), respectively, it is possible to define the adjoint of the controllability operator $\hat{\boldsymbol{L}}_c : L^2(-\infty, 0] \rightarrow \mathbb{U}$ and the observability operator $\hat{\boldsymbol{L}}_o : \mathbb{U} \rightarrow L^2[0, \infty)$. To this end, we introduce the inputs vector $\boldsymbol{t} = (\boldsymbol{z}^*, \boldsymbol{v}^*) \in \mathbb{R}^{(p+k)}$ and the outputs vector $\boldsymbol{e} = \left(\boldsymbol{w}^*, \boldsymbol{\phi}^*, \boldsymbol{g}^*\right) \in \mathbb{R}^{(m+2)}$. The adjoint of the controllability operator $\hat{\boldsymbol{L}}_c^* : \mathbb{U} \rightarrow L^2(-\infty, 0]$ maps an initial adjoint state $\boldsymbol{p}_0 \in \mathbb{U}$ to a signal $\boldsymbol{e}$ at time $-t$:

$$\boldsymbol{e}(-t) = \hat{\boldsymbol{L}}_c^* \boldsymbol{p}_0 = \hat{\boldsymbol{B}}^* \boldsymbol{T}^*(-t) \boldsymbol{p}_0. \tag{C9}$$

The adjoint of the observability operator $\hat{\boldsymbol{L}}_o^* : \hat{L}^2[0, \infty) \rightarrow \mathbb{U}$ drives the input signal $\boldsymbol{t}$ to the reference state $\boldsymbol{p}_0$:

$$\boldsymbol{p}_0 = \hat{\boldsymbol{L}}_o^* \boldsymbol{t}(t) = \int_0^\infty \boldsymbol{T}^*(s) \hat{\boldsymbol{C}}^* \boldsymbol{t}(s) \, \mathrm{d}s. \tag{C10}$$

The direct mapping from the inputs $\boldsymbol{t}$ to the outputs $\boldsymbol{e}$ can be obtained combining $\hat{\boldsymbol{L}}_o^*$ and $\hat{\boldsymbol{L}}_c^*$; the adjoint Hankel $\hat{\boldsymbol{H}}^* : L^2[0, \infty) \rightarrow L^2(-\infty, 0]$ operator is thus defined as

$$\boldsymbol{e}(-t) = \hat{\boldsymbol{H}}^* \boldsymbol{t}(t) = \hat{\boldsymbol{L}}_c^* \hat{\boldsymbol{L}}_o^* \boldsymbol{t}(t) = \int_0^\infty \hat{\boldsymbol{B}}^* \boldsymbol{T}^*(s - t) \, \hat{\boldsymbol{C}}^* \boldsymbol{t}(s) \, \mathrm{d}s. \tag{C11}$$

Finally, introducing $\hat{\boldsymbol{B}}^*$ and $\hat{\boldsymbol{C}}^*$ in the initial-value problem (A 4), the dual input–output system can be defined as

$$-\dot{\boldsymbol{p}} = \hat{\boldsymbol{A}}^* \boldsymbol{p} + \hat{\boldsymbol{C}}^* \boldsymbol{t}, \tag{C12}$$

$$\boldsymbol{e} = \hat{\boldsymbol{B}}^* \boldsymbol{p}. \tag{C13}$$

In the adjoint system, the roles of $\hat{\boldsymbol{B}}$ and $\hat{\boldsymbol{C}}$ have been exchanged: the system is now forced by the outputs $\boldsymbol{t}$, while the inputs are extracted as measurements.

C.2. *Balanced modes*

Using the Hankel operator and the related adjoint operator, we can quantify the output energy obtained from a past input $\boldsymbol{f}(t)$ by

$$\|\boldsymbol{y}\|^2_{L^2[0,\infty)} = \langle \hat{\boldsymbol{H}} \boldsymbol{f}, \hat{\boldsymbol{H}} \boldsymbol{f} \rangle_{L^2[0,\infty)} = \langle \boldsymbol{f}, \hat{\boldsymbol{H}}^* \hat{\boldsymbol{H}} \boldsymbol{f} \rangle_{L^2(-\infty,0]}. \tag{C14}$$

If a given input forcing $\boldsymbol{f}_i(t)$ is a unit-norm eigenvector of $\hat{\boldsymbol{H}}^* \hat{\boldsymbol{H}}$, then the output energy will be given by the square of the corresponding Hankel singular value (HSV) σ_i:

$$\hat{\boldsymbol{H}}^* \hat{\boldsymbol{H}} \boldsymbol{f}_i(t) = \sigma_i^2 \boldsymbol{f}_i(t). \tag{C15}$$

The HSVs are real and positive; thus, they can be ranked according to the associated energy amplification. Multiplying (C15) from left with $\hat{\boldsymbol{L}}_c$, we get

$$\hat{\boldsymbol{L}}_c\hat{\boldsymbol{H}}^*\hat{\boldsymbol{H}}\boldsymbol{f}_i(t) = \underbrace{\hat{\boldsymbol{L}}_c\hat{\boldsymbol{L}}_c^*}_{\boldsymbol{P}}\underbrace{\hat{\boldsymbol{L}}_o^*\hat{\boldsymbol{L}}_o}_{\boldsymbol{Q}}\underbrace{\hat{\boldsymbol{L}}_c\boldsymbol{f}_i}_{\sigma_i\boldsymbol{\phi}_i} = \sigma_i^2(\sigma_i\boldsymbol{\phi}_i), \tag{C16}$$

where we have defined the balanced mode $\boldsymbol{\phi}_i$ associated with σ_j as

$$\boldsymbol{\phi}_i = \frac{1}{\sigma_i}\hat{\boldsymbol{L}}_c\boldsymbol{f}_i, \tag{C17}$$

and the controllability Gramian $\boldsymbol{P}$ and the observability Gramian $\boldsymbol{Q}$ as

$$\boldsymbol{P} = \hat{\boldsymbol{L}}_c\hat{\boldsymbol{L}}_c^* = \int_0^\infty \boldsymbol{T}(\tau)\hat{\boldsymbol{B}}\hat{\boldsymbol{B}}^*\boldsymbol{T}^*(\tau)\,\mathrm{d}\tau, \tag{C18a}$$

$$\boldsymbol{Q} = \hat{\boldsymbol{L}}_o^*\hat{\boldsymbol{L}}_o = \int_0^\infty \boldsymbol{T}^*(\tau)\hat{\boldsymbol{C}}^*\hat{\boldsymbol{C}}\boldsymbol{T}(\tau)\,\mathrm{d}\tau. \tag{C18b}$$

The balanced modes are thus the eigenvectors of the product of the observability $\boldsymbol{Q}$ and controllability Gramians $\boldsymbol{P}$, written in matrix form,

$$(\boldsymbol{P}\boldsymbol{Q})\boldsymbol{\Phi} = \boldsymbol{\Phi}\Sigma^2, \tag{C19}$$

$\boldsymbol{\Phi} = (\boldsymbol{\phi}_1, \boldsymbol{\phi}_2, \ldots, \boldsymbol{\phi}_r)$ and $\Sigma^2 = \mathrm{diag}\{\sigma_1^2, \ldots, \sigma_r^2\}$. The set of left eigenvectors of $\boldsymbol{P}\boldsymbol{Q}$ represents the adjoint balanced modes set, hereafter denoted by $\boldsymbol{\Psi}$.

Two main reasons make the model reduction obtained by projection onto balanced modes particularly convenient.

(*a*) The reduced-order system is guaranteed to be asymptotically stable if $\sigma_j \neq \sigma_{j+1}$ for all j (Pernebo & Silverman 1982).

(*b*) Tight error bounds exist (Glover 1984),

$$\sigma_{r+1} \leqslant \|\hat{\boldsymbol{G}} - \hat{\boldsymbol{G}}_r\|_\infty \leqslant 2\sum_{j=r+1}^{n}\sigma_j, \tag{C20}$$

where $\hat{\boldsymbol{G}}$ and $\hat{\boldsymbol{G}}_r$ are the input–output systems associated with (3.1) and (3.6), respectively, and $\|\hat{\boldsymbol{G}} - \hat{\boldsymbol{G}}_r\|_\infty$ is the infinity norm. More details about the operators introduced in the identification of the balanced mode are given by Glover (1984) and Dullerud & Paganini (1999).

C.3. *Snapshot method*

An essential ingredient in the computation of the balanced modes is the identification of the Gramians $\boldsymbol{P}$ and $\boldsymbol{Q}$, usually evaluated as solution of Lyapunov equations (Green & Limebeer 1995). Unfortunately, the solution of the Lyapunov equations involves a computational complexity $O(n^3)$ and a storage requirement $O(n^2)$, making it unfeasible for high-dimensional systems (Laub *et al.* 1987). An alternative is given by the *snapshot method* (Rowley 2005), where empirical Gramians are computed using the following quadratures:

$$\hat{\boldsymbol{P}} \approx \sum_{j=1}^{n_t}\boldsymbol{T}(t_j)\hat{\boldsymbol{B}}\hat{\boldsymbol{B}}^*\boldsymbol{T}^*(t_j)\delta_j = \boldsymbol{X}\boldsymbol{X}^*, \tag{C21a}$$

$$\hat{\boldsymbol{Q}} \approx \sum_{j=1}^{n_t}\boldsymbol{T}^*(t_j)\hat{\boldsymbol{C}}^*\hat{\boldsymbol{C}}\boldsymbol{T}(t_j)\delta_j = \boldsymbol{Y}^*\boldsymbol{Y}. \tag{C21b}$$

Here, δ_j are the time quadrature weights, n_t the number of samplings, $\boldsymbol{X} \in \mathbb{R}^{n \times n_t m}$ and $\boldsymbol{Y} \in \mathbb{R}^{n \times n_t p}$ are the Cholesky factors:

$$\boldsymbol{X} = [\boldsymbol{T}(t_1)\hat{\boldsymbol{B}}\sqrt{\delta_1}, \boldsymbol{T}(t_2)\hat{\boldsymbol{B}}\sqrt{\delta_2}, \ldots, \boldsymbol{T}(t_k)\hat{\boldsymbol{B}}\sqrt{\delta_{n_t}}], \tag{C22a}$$

$$\boldsymbol{Y} = [\boldsymbol{T}^*(t_1)\hat{\boldsymbol{C}}^*\sqrt{\delta_1}, \boldsymbol{T}^*(t_2)\hat{\boldsymbol{C}}^*\sqrt{\delta_2}, \ldots, \boldsymbol{T}^*(t_k)\hat{\boldsymbol{C}}^*\sqrt{\delta_{n_t}}]. \tag{C22b}$$

Each element of the Cholesky factor $\boldsymbol{X}$ contains snapshots of the flow field computed by the impulse response to each input $\hat{\boldsymbol{B}}_i$ at a given time t_j. Similarly, the Cholesky factor $\boldsymbol{Y}$ can be obtained by gathering the snapshots computed by marching backwards in time with the adjoint system (A 3). Please note that the number of collected snapshots is n_t times the number of inputs (m) and outputs (p).

Using the low-rank Cholesky factors, the approximate direct and adjoint balanced modes can be computed as follows. As a first step, the singular value decomposition of $\boldsymbol{Y}^*\boldsymbol{X}$ is formed:

$$\boldsymbol{Y}^*\boldsymbol{X} = \boldsymbol{U}\boldsymbol{\Sigma}\boldsymbol{V}^*. \tag{C23}$$

The size of $\boldsymbol{Y}^*\boldsymbol{X}$ is $n_t p \times n_t m$; as long as the number of degree of freedom n is smaller than the number of collected snapshots, the method is cheaper than the standard method (using full Cholesky factors of size $n \times n$) . The diagonal matrix $\boldsymbol{\Sigma}$ contains the approximate HSVs. The direct and adjoint balanced modes are then given by

$$\boldsymbol{\Phi}_r = \boldsymbol{X}\boldsymbol{V}\boldsymbol{\Sigma}^{-1/2}, \quad \boldsymbol{\Psi}_r = \boldsymbol{Y}^*\boldsymbol{U}\boldsymbol{\Sigma}^{-1/2}. \tag{C24}$$

Here, only time quadrature weights were considered; however, note that spatial integral weights are introduced when inner product are computed, see Bagheri *et al.* (2009*b*). In general, numerical tests (Ilak & Rowley 2008; Ahuja 2009; Bagheri *et al.* 2009*a*) have shown that the approximate balanced modes are a good approximation to exact balancing modes and that Σ_r are close to the true HSVs. This can be attributed to the low numerical rank of the Gramians, when $m, p \ll n$.

REFERENCES

Ahuja, S. 2009 Reduction methods for feedback stabilization of fluid flows. PhD thesis, Princeton University, New Jersey.

Ahuja, S. & Rowley, C. W. 2010 Feedback control of unstable steady states of flow past a flat plate using reduced-order estimators. *J. Fluid Mech.* **645**, 447–478.

Åkervik, E., Ehrenstein, U., Gallaire, F. & Henningson, D. S. 2008 Global two-dimensional stability measures of the flat plate boundary-layer flow. *Eur. J. Mech.* B/*Fluids* **27**, 501–513.

Anderson, B. & Moore, J. 1990 *Optimal Control: Linear Quadratic Methods*. Prentice Hall.

Bagheri, S., Åkervik, E., Brandt, L. & Henningson, D. S. 2009*a* Matrix-free methods for the stability and control of boundary layers. *AIAA J.* **47**, 1057–1068.

Bagheri, S., Brandt, L. & Henningson, D. S. 2009*b* Input–output analysis, model reduction and control design of the flat-plate boundary layer. *J. Fluid Mech.* **620**, 263–298.

Bagheri, S., Hœpffner, J., Schmid, P. J. & Henningson, D. S. 2009*c* Input–output analysis and control design applied to a linear model of spatially developing flows. *Appl. Mech. Rev.* **62** (2), 1–27.

Bamieh, B., Paganini, F. & Dahleh, M. 2002 Distributed control of spatially invariant systems. *IEEE Trans. Autom. Control* **47** (7), 1091–1107.

Barbagallo, A., Sipp, D. & Schmid, P. J. 2009 Closed-loop control of an open cavity flow using reduced-order models. *J. Fluid Mech.* **641**, 1–50.

Bewley, T. R. 2001 Flow control: new challenges for a new renaissance. *Prog. Aerosp. Sci.* **37**, 21–58.

Bewley, T. R. & Liu, S. 1998 Optimal and robust control and estimation of linear paths to transition. *J. Fluid Mech.* **365**, 305–349.

Bewley, T. R., Moin, P. & Temam, R. 2001 DNS-based predictive control of turbulence: an optimal benchmark for feedback algorithms. *J. Fluid Mech.* **447**, 179–225.

Butler, K. & Farrell, B. F. 1992 Three-dimensional optimal perturbations in viscous shear flow. *Phys. Fluids* A **4**, 1637–1650.

Chevalier, M., Hœpffner, J., Åkervik, E. & Henningson, D. S. 2007*a* Linear feedback control and estimation applied to instabilities in spatially developing boundary layers. *J. Fluid Mech.* **588**, 163–187.

Chevalier, M., Hœpffner, J., Bewley, T. R. & Henningson, D. S. 2006 State estimation in wall-bounded flow systems. Part 2. Turbulent flows. *J. Fluid Mech.* **552**, 167–187.

Chevalier, M., Schlatter, P., Lundbladh, A. & Henningson, D. S. 2007*b* A pseudo-spectral solver for incompressible boundary layer flows. Trita-Mek 7. KTH Mechanics, Stockholm, Sweden.

Choi, H., Moin, P. & Kim, J. 1993 Direct numerical simulation of turbulent flow over riblets. *J. Fluid Mech.* **255**, 503–539.

Chomaz, J. M. 2005 Global instabilities in spatially developing flows: Non-normality and nonlinearity. *Annu. Rev. Fluid Mech.* **37**, 357–392.

Cortelezzi, L., Speyer, J. L., Lee, K. H. & Kim, J. 1998 Robust reduced-order control of turbulent channel flows via distributed sensors and actuators. In *IEEE 37th Conf. on Decision and Control,* pp. 1906–1911.

Curtain, R. & Zwart, H. 1995 *An Introduction to Infinite-Dimensional Linear Systems Theory*. Springer.

Doyle, J. C. 1978 Guaranteed margins for LQG regulators. *IEEE Trans. Autom. Control* **23**, 756–757.

Doyle, J. C., Glover, K., Khargonekar, P. P. & Francis, B. A. 1989 State-space solutions to standard H_2 and H_∞ control problems. *IEEE Trans. Autom. Control* **34**, 831–847.

Dullerud, E. G. & Paganini, F. 1999 *A Course in Robust Control Theory. A Convex Approach*. Springer Verlag.

Glover, K. 1984 All optimal Hankel-norm approximations of linear multivariable systems and the l^∞-error bounds. *Intl J. Control* **39**, 1115–1193.

Green, M. & Limebeer, J. N. 1995 *Linear Robust Control*. Prentice Hall.

Grundmann, S. & Tropea, C. 2008 Active cancellation of artificially introduced Tollmien–Schlichting waves using plasma actuators. *Exp. Fluids* **44** (5), 795–806.

Hammond, E. P., Bewley, T. R. & Moin, P. 1998 Observed mechanisms for turbulence attenuation and enhancement in opposition-controlled wall-bounded flows. *Phys. Fluids* **10** (9), 2421–2423.

Ho, C. M. & Tai, Y. 1998 Micro-electro-mechanical systems MEMS and fluid flows. *Annu. Rev. Fluid Mech.* **30**, 579–612.

Högberg, M. & Bewley, T. R. 2000 Spatially localized convolution kernels for feedback control of transitional flows. In *IEEE 39th Conf. on Decision and Control,* pp. 3278–3283.

Högberg, M., Bewley, T. R. & Henningson, D. S. 2003*a* Linear feedback control and estimation of transition in plane channel flow. *J. Fluid Mech.* **481**, 149–175.

Högberg, M., Bewley, T. R. & Henningson, D. S. 2003*b* Relaminarization of $Re_\tau = 100$ turbulence using gain scheduling and linear state-feedback control flow. *Phys. Fluids* **15**, 3572–3575.

Holmes, P., Lumley, J. & Berkooz, G. 1996 *Turbulence Coherent Structures, Dynamical Systems and Symmetry*. Cambridge University Press.

Ilak, M., Bagheri, S., Brandt, L., Rowley, C. W. & Henningson, D. 2010 Model reduction of the nonlinear complex Ginzburg–Landau equation. *SIAM J. Appl. Dyn. Syst.* **9** (4), 1284–1302.

Ilak, M. & Rowley, C. W. 2008 Modeling of transitional channel flow using balanced proper orthogonal decomposition. *Phys. Fluids* **20**, 034103.

Joshi, S. S., Speyer, J. L. & Kim, J. 1997 A systems theory approach to the feedback stabilization of infinitesimal and finite-amplitude disturbances in plane Poiseuille flow. *J. Fluid Mech.* **332**, 157–184.

Kalman, R. E. 1960 A new approach to linear filtering and prediction problems. *Trans. ASME* D *J. Basic Engng* **82**, 24–45.

Laub, A. 1991 Invariant subspace methods for the numerical solution of Riccati equations. In *The Riccati Equation* (ed. S. Bittaini, A. J. Laub & J. C. Willems), pp. 163–196. Springer.

Laub, A., Heath, M., Paige, C. & Ward, R. 1987 Computation of system balancing transformations and other applications of simultaneous diagonalization algorithms. *IEEE Trans. Autom. Control* **32** (2), 115–122.

Lewis, F. L. & Syrmos, L. V. 1995 *Optimal Control*. Wiley.

Lundell, F. 2003 Pulse-width modulated blowing/suction as a flow control actuator. *Exp. Fluids* **35**, 502–504.

Lundell, F. 2007 Reactive control of transition induced by free-stream turbulence: an experimental demonstration. *J. Fluid Mech.* **585**, 41–71.

Ma, Z., Ahuja, S. & Rowley, C. W. 2009 Reduced order models for control of fluids using the eigensystem realization algorithm. *Theor. Comput. Fluid Dyn.* (in press).

Milling, W. 1981 Tollmien–Schlichting wave cancellation. *Phys. Fluids* **24** (5), 979–981.

Monokrousos, A., Åkervik, E., Brandt, L. & Henningson, D. S. 2010*a* Global optimal disturbances in the Blasius boundary-layer flow using time-steppers. *J. Fluid Mech.* **650**, 181–214.

Monokrousos, A., Brandt, L., Schlatter, P. & Henningson, D. S. 2008 DNS and LES of estimation and control of transition in boundary layers subject to free-stream turbulence. *Intl J. Heat Fluid Flow* **29** (3), 841–855.

Monokrousos, A., Lundell, F. & Brandt, L. 2010*b* Feedback control of boundary layer bypass transition: comparison of a numerical study with experiments. *J. AIAA* **48** (8), 1848–1851.

Moore, B. 1981 Principal component analysis in linear systems: controllability, observability, and model reduction. *IEEE Trans. Autom. Control* **26** (1), 17–32.

Nordström, J., Nordin, N. & Henningson, D. S. 1999 The fringe region technique and the Fourier method used in the direct numerical simulation of spatially evolving viscous flows. *SIAM J. Sci. Comput.* **20** (4), 1365–1393.

Pang, J. & Choi, K.-S. 2004 Turbulent drag reduction by Lorentz force oscillation. *Phys. Fluids* **16** (5), L35–L38.

Pernebo, L. & Silverman, L. 1982 Model reduction via balanced state space representations. *IEEE Trans. Autom. Control* **27**, 382–387.

Quadrio, M. & Ricco, P. 2004 Critical assessment of turbulent drag reduction through spanwise wall oscillations. *J. Fluid Mech.* **521**, 251–271.

Rempfer, D. & Fasel, H. 1994 Evolution of three-dimensional coherent structures in a flat-plate boundary layer. *J. Fluid. Mech.* **260**, 351–375.

Rowley, C. W. 2005 Model reduction for fluids using balanced proper orthogonal decomposition. *Intl J. Bifurcation Chaos* **15** (3), 997–1013.

Schlichting, H. & Gersten, K. 2000 *Boundary-Layer Theory*. Springer.

Semeraro, O., Bagheri, S., Brandt, L. & Henningson, D. S. 2010 Linear control of 3D disturbances on a flat-plate. In *Seventh IUTAM Symp. on Laminar–Turbulent Transition* (ed. P. Schlatter & D. S. Henningson), vol. 18. Springer.

Skogestad, S. & Postlethwaite, I. 2005 *Multivariable Feedback Control, Analysis to Design*, 2nd edn. Wiley.

Smith, B. L. & Glezer, A. 1998 The formation and evolution of synthetic jets. *Phys. Fluids* **10** (9), 2281–2297.

Sturzebecher, D. & Nitsche, W. 2003 Active cancellation of Tollmien–Schlichting waves instabilities on a wing using multi-channel sensor actuator systems. *Intl J. Heat Fluid Flow* **24**, 572–583.

Tempelmann, D., Hanifi, A. & Henningson, D. S. 2010 Optimal disturbances and receptivity in three-dimensional boundary layers. In *5th European Conf. on Computational Fluid Dynamics*, *Lisbon, Portugal.*

White, E. & Saric, W. 2000 Application of variable leading-edge roughness for transition control on swept wings. In *38th AIAA Aerospace Sciences Meeting and Exhibit*. *AIAA Paper* 2000-283. Reno, NV.

Zhou, K., Doyle, J. C. & Glover, K. 2002 *Robust and Optimal Control*. Prentice Hall.

Zhou, K., Salomon, G. & Wu, E. 1999 Balanced realization and model reduction for unstable systems. *Intl J. Robust Nonlinear Control* **9**, 183–198.